

## “PROPELLER” REGIME OF DISK ACCRETION TO RAPIDLY ROTATING STARS

G.V. USTYUGOVA

Keldysh Institute of Applied Mathematics, Russian Academy of Sciences, Moscow, Russia; ustyugg@spp.Keldysh.ru

A.V. KOLDOBA

Institute of Mathematical Modeling, Russian Academy of Sciences, Moscow, Russia; koldoba@spp.Keldysh.ru

M.M. ROMANOVA

Department of Astronomy, Cornell University, Ithaca, NY 14853-6801; romanova@astro.cornell.edu

R.V.E. LOVELACE

Department of Astronomy, Department of Applied and Engineering Physics, Cornell University, Ithaca, NY 14853-6801; RVL1@cornell.edu

*Subject headings:* accretion, dipole — magnetic fields — stars: magnetic fields — X-rays: stars

*Draft version April 3, 2019*

### ABSTRACT

We present results of axisymmetric magnetohydrodynamic simulations of the interaction of a rapidly rotating, magnetized star with an accretion disk. The disk is considered to have a finite viscosity and magnetic diffusivity. The main parameters of the system are the star’s angular velocity and magnetic moment, and the disk’s viscosity and diffusivity. We focus on the “propeller” regime where the inner radius of the disk is larger than the corotation radius. Two types of magnetohydrodynamic flows have been found as a result of simulations: “weak” and “strong” propellers. The strong propellers are characterized by a powerful disk wind and a collimated magnetically dominated outflow or jet from the star. The weak propellers have only weak outflows. We investigated the time-averaged characteristics of the interaction between the main elements of the system, the star, the disk, the wind from the disk, and the jet. Rates of exchange of mass and angular momentum between the elements of the system are derived as a function of the main parameters. The propeller mechanism may be responsible for the fast spinning-down of the classical T Tauri stars in the initial stages of their evolution, and for the spinning-down of accreting millisecond pulsars.

### 1. INTRODUCTION

This work studies the interaction of a rapidly rotating magnetized star with an accretion disk under conditions where the corotation radius of the star,  $r_c = (GM/\Omega_*^2)^{1/3}$ , is less than the inner radius of the disk,  $r_d$ . The radius  $r_d$  is determined by the star’s magnetic field and angular velocity as well as the mass accretion rate of the disk  $\dot{M}$  and the disk viscosity and magnetic diffusivity. Disk accretion is disrupted for radii  $\lesssim r_d$ . At distances  $\sim r_d$  the disk plasma acquires additional angular velocity due to “friction” with the magnetosphere of the star which rotates faster than the Keplerian motion of the disk. The behavior of the matter at  $r_d$  depends on the ratio between angular velocity of the star and Keplerian angular velocity at  $r_d$ . The matter tends to be expelled from the disk if the centrifugal force is sufficiently larger than the gravitational force. This regime of interaction between a magnetized star and an accretion disk is called “propeller” regime (Illarionov & Sunyaev 1975). This regime was investigated analytically (e.g., Davies, Fabian, & Pringle 1979; Lovelace, Romanova, & Bisnovatyi-Kogan 1999, hereafter - LRBK99; Ikhsanov 2002; Rappaport, Fregeau, & Spruit 2004; Eksi, Hernquist, & Narayan 2005), and numerically (Romanova et al. 2004b - hereafter RUKL04; Romanova et al. 2005 - hereafter RUKL05).

In the disk-magnetosphere interaction the magnetic field plays the main role in two processes. Firstly, it disrupts the inner regions of the disk and thus determines the inner

radius of the disk. Secondly, the magnetic field determines the direction of plasma flow. Matter of the disk at a distance  $r$  is accelerated in the azimuthal direction if it is threaded by field lines connecting it with a star rotating more rapidly than the disk; that is  $r > r_c$ . In the opposite case where  $r < r_c$ , the azimuthal motion of the disk matter is slowed down. In the first case the disk plasma gains angular momentum from the star and moves outward. In second case the disk plasma loses angular momentum and moves inward. Thus, in the inner regions of the disk the action of magnetic field leads to enhanced accretion rate, while in the outer regions to reduced accretion or even to outflow of matter.

The disk-magnetosphere interaction depends essentially on the ratio of the inner radius of the disk  $r_d$  to the corotation radius  $r_c$ . In the model studied here the location of the radius  $r_d$  depends mainly on the magnetic field of the star and the disk accretion rate. In the absence of external plasma the magnetic field of the star is considered to be a dipole field with the magnetic moment  $\mu$  parallel to the rotational axis. Consequently the magnetic stresses are proportional to  $r^{-6}$ .

For  $r_d \lesssim r_c$ , disruption of the disk is accompanied by the formation of “funnel flows” (e.g., Ghosh & Lamb 1978; Königl 1991; Shu et al. 1994). Funnel flows were recently investigated numerically using 2D and 3D MHD simulations (Romanova et al. 2002, 2003, 2004a). In this paper we consider the opposite limit where  $r_d \gtrsim r_c$ . In this limit one expects that the closed field region of the star will con-

tain relatively low-density plasma rotating with the star's angular velocity. Outside of this region there is a relatively dense disk plasma threaded by open magnetic field lines. Interaction between the two regions occurs by two processes: (1) by matter flow from open field lines to the closed field lines as a result of magnetic diffusivity; and (2) angular momentum exchange between fast rotating matter of magnetosphere and slowly rotating disk. The first process can lead to penetration of significant amounts of matter with low angular momentum to the closed field lines. This can in turn lead to significant deformation of the field lines and possibly to their opening. The second process may lead to azimuthal acceleration of the disk matter sufficient to stop the accretion and to eject matter from the disk. An outflow from the system may occur.

This paper treats disk accretion to a rotating magnetized star using magnetohydrodynamics. For the initial set up of the system we divide the space into the “disk” and the “corona” with a smooth transition between them. The disk is relatively cold and dense while the opposite is true for the corona. The disk and corona are separated by a specified level of density. In the disk we take into account viscosity and magnetic diffusivity of the plasma.

We consider that both the viscosity and the magnetic diffusivity of the disk plasma are due to turbulent fluctuations of the velocity and magnetic field. We adopt the standard hypotheses where the molecular transport coefficients are substituted with the turbulent coefficients. To estimate the value of these coefficients, we use the  $\alpha$ -model of Shakura and Sunyaev (1973) where the coefficient of the turbulent kinematic viscosity  $\nu_t = \alpha_v c_s^2 / \Omega_K$ , where  $c_s$  is the isothermal sound speed and  $\Omega_K$  is the Keplerian angular velocity at the given location. Similarly, the coefficient of the turbulent magnetic diffusivity  $\eta_t = \alpha_d c_s^2 / \Omega_K$ . Here,  $\alpha_v$  and  $\alpha_d$  are dimensionless coefficients which are treated as parameters of the model.

Our numerical simulations have shown that the MHD flows which appear as a result of interaction between a rapidly rotating magnetized star and accretion disk can be divided to two types: “weak” and “strong” propeller. In the first case, no outflows are observed (RUKL04), while in the second case a large fraction of the mass accretion of the disk goes to the outflows (RUKL05). In this paper we investigate regime of “strong” propellers in detail.

The inner disk radius  $r_d$  is determined by the disk interaction with the magnetized star. The value  $r_d$  varies with time significantly. We can consider however an average value of  $r_d$ . This value depends on the parameters of the model which characterize both the star, its mass  $M$ , magnetic moment  $\mu$ , and angular velocity  $\Omega_*$ ; and the disk, the coefficients of viscosity and magnetic diffusivity, density, temperature and connected with them the accretion rate in the disk. The corona may also have a significant role. In order to decrease the influence of corona we have taken its density to be as low as possible.

From the parameters of the model we can construct in addition to the corotation radius another important length termed the nominal Alfvén radius,  $r_A \equiv [\mu^4 / (GM\dot{M}^2)]^{1/7}$  (e.g., Davidson & Ostriker 1973). Here,  $\dot{M}$  is the disk accretion rate at large distances, which can be obtained from the simulations. Another characteristic length can be obtained from the following. Close to the star the magnetic

field dominates, that is, the magnetic pressure is larger than the  $\phi\phi$  component of the momentum tensor of the matter  $\rho v_\phi^2 + p$ . Inside the region where the magnetic field dominates, the plasma flow is controlled by the magnetic field and the flow is along the magnetic field lines. The boundary of this region follows from  $p + \rho v_\phi^2 = \mathbf{B}^2 / 8\pi$ . This surface intersects the equatorial region along the circle with the radius  $r_m$ , which we will call the magnetospheric radius.

The strength of the propeller is determined by the value of the dimensionless ratio,  $r_A/r_c$  or  $r_m/r_c$ , and also by other dimensionless parameters of the model such as the  $\alpha$ -coefficients of the viscosity and magnetic diffusivity. The characteristic feature of the disk-magnetosphere interaction in the strong propeller regime is the formation of an outflow of the disk matter along the opened magnetic field lines. This outflow is termed the “wind.” The matter outflows are strongest in the vicinity of the neutral line of the poloidal field, which starts approximately at the inner radius of the disk. This is the region of the most intense angular momentum transport from the fast rotating magnetosphere to the disk due to “viscous” stresses. At the same time there is a magnetically dominated (Poynting) “jet” which flows out along the opened magnetic field lines extending outward from the star. The wind has a large inclination angle relative to the rotational axis and for a very strong propeller it flows almost along the disk surface. In contrast, the jet becomes more collimated as the strength of the propeller increases. As the strength increases there is a sharp decrease of the accretion rate to the star.

Section 2 discusses theoretical approach to the problem. Section 3 discusses our numerical model. Section 4 discusses results and Section 5 summarizes the work.

## 2. STRUCTURE AND EVOLUTION OF THE DISK WITH MAGNETIC FIELD

### 2.1. Non-Magnetic Disk

For a stationary non-magnetic thin disk, the fluxes of matter  $\dot{M}$  and angular momentum  $\dot{L}$  are conserved along the disk (see, e.g., Kato, Fukue & Mineshige 1988; Lipunov 1992)

$$\begin{aligned} r\Sigma V_r &= -\frac{\dot{M}}{2\pi} = \text{const} , \\ r^2(\Sigma V_r V_\phi + \tau) &= -\frac{\dot{L}}{2\pi} = \text{const} . \end{aligned} \quad (1)$$

Here,  $\Sigma = \int dz \rho$  is the surface density;  $\tau = \int dz \tau_{r\phi}$  is the “viscous” stress acting in the disk,  $V_r$  and  $V_\phi$  are components of the flow velocity. Here,  $\dot{M} > 0$  is the inward mass flux, and  $\dot{L} > 0$  is the inward angular momentum flux. From equations (1) we obtain

$$\tau = \frac{1}{2\pi} \left( \dot{M}\Omega - \frac{\dot{L}}{r^2} \right) = \frac{\dot{M}}{2\pi} \left( \Omega - \frac{\lambda}{r^2} \right) . \quad (2)$$

Here,  $\Omega \equiv V_\phi/r$  is the angular velocity of the disk, and  $\lambda \equiv \dot{L}/\dot{M} > 0$  is an angular momentum per unit mass of the accretion flow. The viscous stresses are typically very small at the inner radius of the disk where the motion departs significantly from Keplerian. The inner radius of the

disk determined by this way is  $r_i \approx \lambda^2/GM$ . The “viscous” stresses are determined by processes of turbulent fluctuations which are not fully understood. A simplified approach is commonly adopted where the  $r\phi$ -component of the viscous stress tensor (integrated over  $z$ ) is expressed as  $\tau = -\nu_t \Sigma r \partial \Omega / \partial r$ , where  $\nu_t$  is coefficient of turbulent viscosity. In the region of quasi-Keplerian disk ( $\Omega \approx \Omega_K$ )

$$\begin{aligned} \tau &= \frac{3}{2} \nu_t \Sigma \Omega_K, \\ V_r &= -\frac{3\nu_t}{2r}, \\ \Sigma &= \frac{\dot{M}}{3\pi\nu_t}. \end{aligned} \quad (3)$$

Three-dimensional simulations of the local regions of Keplerian disks indicate that the viscous stress  $\tau$  constitutes a fraction of the gas pressure (integrated over  $z$ ) in the disk. Namely,  $\tau = (3\alpha_v/2)\Pi = (3\alpha_v/2) \int dz p$ , where  $\alpha_v$  is a dimensionless coefficient. The value of  $\alpha_v$  is in the rough interval  $3 \times 10^{-3} - 0.4$  (Balbus 2003). Comparing the last expression and (3), we obtain the Shakura-Sunyaev formulae  $\nu_t = \alpha_v c_s^2 / \Omega_K$ , where  $c_s^2 = \Pi / \Sigma$  is an average isothermal speed in the disk.

Equations (3) show that the radial accretion speed is determined by local properties of the disk. The surface density  $\Sigma$  is set by the local properties as well as the global quantity, the accretion rate  $\dot{M}$ . The same is true for the nominal inner radius of the disk  $r_i$ , which is determined by the parameter  $\lambda$ . To understand how the processes at the inner edge of the disk influence the global characteristics of accretion process  $\dot{M}$  and  $\dot{L}$ , it is necessary to consider non-stationary processes. The continuity equation gives

$$\frac{\partial \Sigma}{\partial t} + \frac{1}{r} \frac{\partial}{\partial r} (r \Sigma V_r) = 0. \quad (4)$$

Conservation of angular momentum gives

$$\frac{\partial (\Sigma r V_\phi)}{\partial t} + \frac{1}{r} \frac{\partial}{\partial r} [r^2 (\Sigma V_r V_\phi + \tau)] = 0. \quad (5)$$

If  $\Omega \approx \Omega_K$  we obtain

$$r \Sigma V_r = -\frac{1}{d\ell/dr} \frac{\partial (r^2 \tau)}{\partial r} = -\frac{2}{V_K} \frac{\partial (r^2 \tau)}{\partial r}, \quad (6)$$

where  $\ell = \Omega_K r^2$  is specific angular momentum. Taking the first of equations (3),

$$\Sigma = \frac{2}{3} \frac{\tau}{\nu_t \Omega_K},$$

and combining this equation with (4), and (6) we obtain

$$\frac{\partial f}{\partial t} = \frac{3\nu_t}{\sqrt{r}} \frac{\partial}{\partial r} \left( \sqrt{r} \frac{\partial f}{\partial r} \right), \quad (7)$$

where  $f \equiv r^2 \tau$  is the angular momentum flux due to the viscous stress.

The evolution of  $f = r^2 \tau$  is described by a diffusion equation with diffusion coefficient  $\sim \nu_t$ . Thus, perturbations generated for example by the star’s magnetic field

at the inner radius of the disk with periodicity  $\Delta t$  diffuse out to distances  $\Delta r \sim \sqrt{\nu_t \Delta t} \sim c_s \sqrt{\alpha_v \Delta t / \Omega_K}$ . If  $\Delta t \sim 1/\Omega_K$ , then  $\Delta r \sim c_s \sqrt{\alpha_v} / \Omega_K \leq h$ . Thus, disturbances of the inner part of the disk at say  $r_d$  are not expected to influence the more distant parts of the disk at  $r \gtrsim 2r_d$ .

## 2.2. Analytic Model of Disk Accretion in “Propeller” Regime

Here, we consider the influence on the disk of an aligned dipole magnetic field of a rotating star following the treatment of Lovelace, Romanova, and Bisnovatyi-Kogan 1999 (LRBK99).

The balance of mass, angular momentum and energy flows is considered in the region  $AA'CC'$  of Figure 1, where the surface  $AA'$  is along the inner region of the disk, while the surface  $CC'$  is sufficiently far away so that the flow can be considered to be undisturbed by the magnetic field of the star. The star’s mass is  $M$ , magnetic moment  $\mu$ , and angular velocity  $\Omega_*$ . The accretion disk with accretion rate  $\dot{M}$  is located at  $r \geq r_d$  and rotates approximately with Keplerian velocity. The magnetosphere rotates with angular velocity of the star  $\Omega_*$ . It is accepted that the angular momentum flux through the surface  $AA'$  is  $N = \alpha \mu^2 / r^3$ , where  $\alpha$  is a dimensionless constant which is an analogue of  $\alpha$ -coefficient in the model by Shakura-Sunyaev. The inner radius of the disk  $r_d$  is found to be

$$\kappa \left( \frac{r_A}{r_d} \right)^{7/3} = \frac{2\alpha}{3} \frac{r_A^{7/2}}{r_d^2 r_c^{3/2}} - 1. \quad (8)$$

Here,  $r_c = (GM/\Omega_*^2)^{1/3}$  is the corotation radius,  $r_A = (\mu^4/GM\dot{M}^2)^{1/7}$  is the nominal Alfvén radius,  $\kappa \lesssim 1$  is a dimensionless constant. (We have simplified the LRBK99 treatment by taking  $\delta = 0$  in original formulae.)

Equation (8) was obtained under fairly general assumptions. However, the derivation assumed stationary conditions and a specific expression for the wind mass, energy, and angular momentum outflow was adopted from Lovelace, Berk, and Contopoulos (1991). Equation (8) implies that the inner radius of the disk  $r_d$  or effective Alfvén radius is determined not only by the mass and magnetic moment of the star and the accretion rate, but also by the star’s angular velocity.

The processes giving the “friction” at the boundary between the inner edge of the disk and magnetosphere is treated phenomenologically by LRBK99 in terms of the dimensionless coefficient  $\alpha$ . The process evidently has a turbulent nature and needs a separate detailed investigation (see, e.g., Rastätter & Schindler 1999).

## 2.3. Disk with Finite Conductivity

The interaction between the magnetized star and the disk depends significantly on the conditions in the corona. Magnetic flux of the star extends into the corona and may thread the disk. We consider the corona to be a perfect conductor. Differential rotation of the foot-points of magnetic field loops threading the star and the disk tend to inflate and open unless there are some opposing factors which suppress this tendency (e.g., Gold & Hoyle 1960; Aly 1980; Lovelace, Romanova & Bisnovatyi-Kogan 1995;

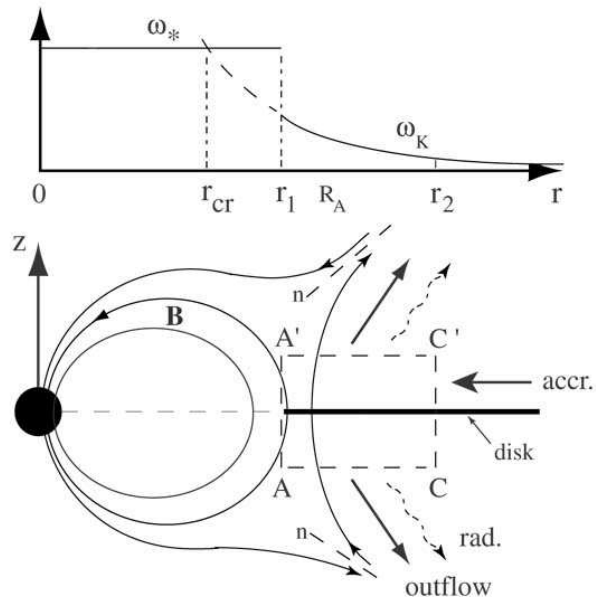


FIG. 1.— Geometry of disk accretion to a rapidly rotating star with an aligned dipole magnetic field. Top panel shows radial distribution of angular velocities of the star and of the disk. Bottom panel shows schematic structure of the magnetosphere in the propeller regime (from Lovelace et al. 1999).

Uzdensky 2002). This was also confirmed by a number of numerical simulations (e.g., Goodson, Böhm & Winglee 1999; Fendt & Elstner 2002).

One factor is the finite conductivity of the disk plasma which leads to reconnection of the inflated field lines (e.g., Aly & Kuijpers 1990; Hayashi, Shibata & Matsumoto 1996; Uzdensky, Königl & Litwin 2002; Yelenina & Ustyugova 2005). A second factor is the density of the corona. A sufficiently dense corona acts to inhibit opening of the magnetic field. Alternatively, a rarefied corona favors the opening of field lines with the coronal field passing through a sequence of force-free configurations. The finite conductivity of the disk leads to the slippage of magnetic field lines relative to the disk matter and thus limits the build up of the toroidal magnetic field. A dense corona acts to oppose twisting of the magnetic field.

We first consider the influence of the finite conductivity of the disk which is assumed to be thin. In a coordinate system attached to a point in the disk Ohm’s law is satisfied in the form  $\mathbf{i} = \lambda \mathbf{E}_t$ , where  $\mathbf{i}$  is the surface current density,  $\mathbf{E}_t$  is the electric field in the plane of the disk, and  $\lambda$  is the “surface conductivity” ( $\int dz \sigma$ ). Thus, in the corona in the non-rotating frame,  $\mathbf{E} = -\mathbf{v} \times \mathbf{B}/c$ , where  $\mathbf{v}$  is the flow velocity in the corona. In the disk,  $\mathbf{i} = \lambda(\mathbf{E} + \mathbf{V} \times \mathbf{B}/c)$ , where  $\mathbf{V}$  is the flow velocity in the disk. These relations can readily be combined to give

$$[(\mathbf{v} - \mathbf{V} + \zeta \hat{\mathbf{z}}) \times \mathbf{B}]_t = 0, \quad (9)$$

on the top side of the disk. Here,  $\zeta \equiv c^2/(2\pi\lambda)$  is the surface magnetic diffusivity,  $\hat{\mathbf{z}}$  is the unit normal to the disk, and index  $t$  shows that at the left-hand-side only tangential to the disk components of vector are important. If we suppose that there is no outflow from the disk ( $v_z = 0$ ), then it follows from (9) that a toroidal magnetic field is

generated at its surface:

$$B_\phi = \frac{v_\phi - V_\phi}{\zeta} B_z. \quad (10)$$

In order to calculate the toroidal magnetic field we make a number of assumptions: First, for the coefficient of magnetic diffusivity we follow the Shakura and Sunyaev  $\alpha$  prescription,  $\eta_t = \alpha_d c_s h$ , here  $c_s$  is an isothermal sound speed (Bisnovatyi-Kogan & Ruzmaiken 1974). Second, the magnetic field in the disk  $B_z$  is taken to be the unperturbed dipole field of the star,  $B_z = \mu/r^3$ . Thirdly, the disk is assumed to rotate with Keplerian angular velocity while the coronal matter above the disk rotates with the angular velocity of the star,  $\Omega_*$ . Neglecting the variations of the tangential electric field  $\mathbf{E}_t$  across the disk, we obtain

$$\frac{1}{\zeta} = \int_{-h}^h \frac{dz}{\eta_t} = \frac{2}{\alpha_d c_s}. \quad (11)$$

Substituting (11) to (10) we obtain

$$B_\phi = \frac{2r}{\alpha_d c_s} (\Omega_* - \Omega_K) B_z = \frac{2\mu}{\alpha_d c_s r^2} (\Omega_* - \Omega_K).$$

For  $\alpha_d \ll 1$  there is a strong twisting of the magnetic field linking the star and the disk,

$$\left| \frac{B_\phi}{B_z} \right| = \frac{2r|\Omega_* - \Omega_K|}{\alpha_d c_s} \gg 1,$$

if the considered distance  $r$  is far from the corotation radius where  $\Omega_* = \Omega_K$ . This equation was derived earlier by Lovelace et al. (1991).

The discontinuity of the azimuthal component of the magnetic field at the disk surface  $z = 0$  means that there is a radial surface current flowing along the disk. The interaction of this current with the vertical magnetic field,  $B_z$ , leads to the loss of angular momentum from both sides

of the disk at the rate  $-2rB_\phi B_z/4\pi$  per unit surface area. For stationary conditions, the conservation of the angular momentum balance gives

$$\frac{1}{r} \frac{\partial}{\partial r} [r^2 (\Sigma V_r V_\phi + \tau)] = \frac{rB_\phi B_z}{2\pi} = \frac{\mu^2}{\pi\alpha_d c_s r^4} (\Omega_* - \Omega_K).$$

Assuming  $\alpha_d, c_s = \text{const}$ , and  $V_\phi = V_K(r)$ , this equation can be integrated to give

$$\tau = \frac{\dot{M}}{2\pi} \left( \Omega_K - \frac{\lambda}{r^2} \right) + \frac{\mu^2}{\pi\alpha_d c_s} \left( \frac{2\sqrt{GM}}{7r^{11/2}} - \frac{\Omega_*}{2r^4} \right), \quad (12)$$

where  $\lambda = \dot{L}/\dot{M}$  is a constant of integration.

We identify the point  $r = r_d$ , where  $\tau = 0$ , with the inner radius of the disk. At this distance the viscous and magnetic stresses lead to significant deviation of rotational velocity from Keplerian. For a sufficiently large magnetic moment and a rapidly rotating star, the deviation from Keplerian motion is determined by the magnetic field. We can then estimate  $r_d$  by comparing the first and the last terms on the right-hand side (12). This gives

$$r_d^{5/2} = \frac{\mu^2 \Omega_*}{\dot{M} \sqrt{GM} \alpha_d c_s} = \frac{r_A^{7/2}}{\alpha_d h_*},$$

where  $r_A = (\mu^4/GM\dot{M}^2)^{1/7}$  is the nominal Alfvén radius and  $h_* = c_s/\Omega_*$  is the hydrostatic thickness of the disk at the corotation radius. Thus,  $r_d = r_A(r_A/\alpha_d h_*)^{2/5} \gg r_A$ . This derivation suggests that  $r_d \gg r_c$  and  $r_d \gg r_i = \lambda^2/GM$ .

In order to estimate the influence of the magnetic field on the disk, we consider a tube of field lines with one foot point frozen to the star and rotating with the angular velocity  $\Omega_*$ , and the other foot-point in the disk rotating with angular velocity  $\Omega \neq \Omega_*$ . The field lines will be deformed due to the differential rotation and this gives rise to an azimuthal magnetic field component. Furthermore, the field lines tend to open as a result of the differential rotation. At the same time the azimuthal component of the field acts in combination with the poloidal field applies a torque to the disk matter. To estimate the net effect on the disk we assume that the opening of the field lines occurs on a time scale  $\Delta t \sim 1/\Delta\Omega$ , where  $\Delta\Omega = |\Omega_* - \Omega|$ . During this time the azimuthal magnetic field builds up to a value  $B_\phi \sim B_z$  at the surface of the disk. The magnetic stress on the disk during this process exerts a torque on the disk (from both sides). The corresponding loss of angular momentum (per unit area) from both sides of the disk is  $\Delta t rB_\phi B_z/2\pi \sim rB_z^2/(2\pi\Delta\Omega)$ . Of course angular momentum per unit area of the disk is simply  $r^2\Sigma\Omega$ . The magnetic field will have a significant influence on the disk when

$$\frac{rB_z^2}{2\pi\Delta\Omega} \gtrsim r^2\Sigma\Omega.$$

Assuming the disk to be roughly Keplerian,  $\Omega \approx \sqrt{GM/r^3}$  with  $\Sigma = \dot{M}/3\pi\nu_t$ , and the magnetic field  $B_z = \mu/r^3$ , we obtain the condition

$$\Omega|\Omega_* - \Omega| \lesssim \frac{\mu^2/r^7}{2\pi\dot{M}/(3\pi\nu_t)} = \frac{3\nu_t}{2} \frac{\mu^2}{\dot{M}r^7}, \quad (13)$$

for the magnetic field to influence the disk motion.

In the limits of slowly and rapidly rotating stars, inequality (13) provides an estimate of the inner radius of the disk: For a slowly rotating star, ( $\Omega_* \ll \Omega$ ),

$$r_d \sim \left( \frac{\alpha_v^2 c_s^4 \mu^4}{G^3 M^3 \dot{M}^2} \right)^{1/7} = r_A \left( \frac{\alpha_v^2 c^4}{G^2 M^2} \right)^{1/7}.$$

For a rapidly rotating star, ( $\Omega_* \gg \Omega$ ),

$$r_d \sim \left( \frac{\alpha_v c^2 \mu^2}{GM\dot{M}\Omega_*} \right)^{1/4}.$$

Here, we have assumed  $\nu_t = \alpha_v c_s^2/\Omega_K$ ,  $\alpha_v = \text{const}$  and dropped insignificant numerical coefficients. The first case corresponds to the situation where the corotation radius  $r_c$  is much larger than the inner disk radius. The second case corresponds to the opposite inequality. In the first case the disruption of the disk occurs in the *Funnel Flow* regime. Matter loses its angular momentum because of “friction” with the slowly rotating magnetosphere and accretes to the star along the dipole field lines, forming the funnel flows. In the second case the disruption of the disk occurs in the *Propeller Regime* where matter acquires angular momentum “friction” with the rotating magnetosphere and is driven away from the star, forming the outflows (jets and winds). Sketches of the flows are shown in the figure 2. Sketches of the radial variation of the disk angular velocity in the equatorial plane in the two cases are shown in Figure 3.

The transition at  $\sim r_d$  between the magnetosphere region which rotates with the angular velocity of the star  $\Omega_*$  and the disk which rotates with Keplerian angular velocity  $\Omega_K$  (more exactly a part of the disk which rotates with quasi-Keplerian velocity) is not sharp, but instead occurs over some distance where instabilities may have a significant role. Instabilities can act generate turbulence at the inner edge of the disk. We expect turbulence will be strongly developed in the “propeller” regime. Figure 4 shows the dependence of the specific angular momentum  $\ell = \Omega r^2$  on radius in the two cases.

One can see that in the “propeller” regime there is a region where  $\partial\ell/\partial r < 0$ , which is the Rayleigh criterion for axisymmetric instability (Chandrasekhar 1961). The decrease of the angular momentum with the distance is only one of the reasons which may give rise to turbulence in the disk. Nevertheless, it is reasonable to expect that the turbulent viscosity and magnetic diffusivity are significantly enhanced at the inner edge of the disk compared with the regions of the Keplerian disk at larger distances.

### 3. FORMULATION OF THE PROBLEM

#### 3.1. Physics Problem

As discussed the nature of the interaction of the magnetized star with the accretion disk depends on many factors. Nevertheless, we can try to classify the resulting configurations basing on the relations between three lengths, the corotation radius  $r_c$ , the magnetospheric radius  $r_m$ , and the inner radius of the disk  $r_d$ . We recall that for  $r_m$  we have in mind the location in the equatorial plane where

$$p + \rho v_\phi^2 = \frac{B^2}{8\pi}. \quad (14)$$

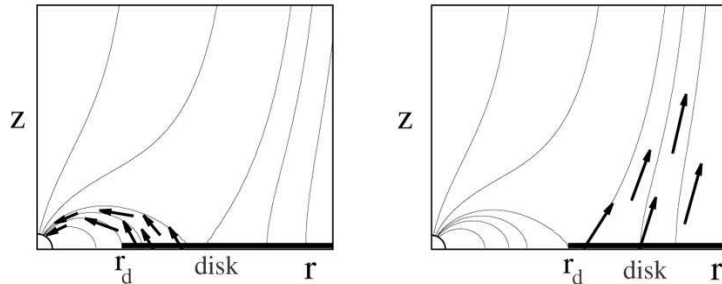


FIG. 2.— Sketches of matter flow in the non-propeller (left panel) and propeller (right panel) cases.

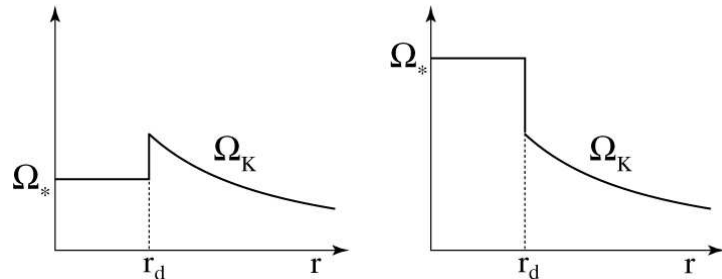


FIG. 3.— Sketches of the radial distribution of the angular velocity in the non-propeller (left panel) and the propeller (right panel) cases.

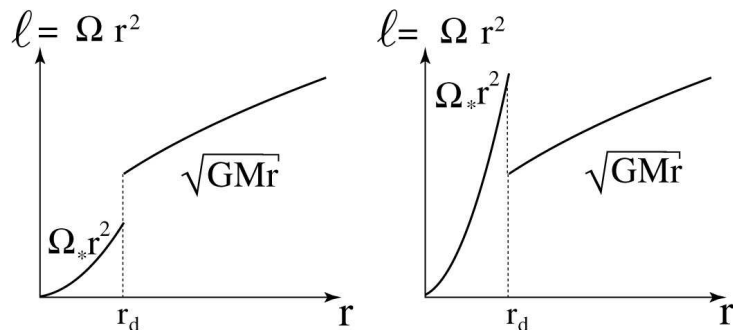


FIG. 4.— Sketches of the radial distribution of the specific angular momentum in the non-propeller (left panel) and propeller (right panel) cases.

It is convenient to use the radius  $r_m$  for comparison with the other two radii even though it depends on the results of simulations. We also note that in the subsequent parts of the paper we will consider only the “propeller” regime. That is, the star is rapidly rotating in the sense that  $r_c < r_d$ . Classification based on the ratio between  $r_d$  and  $r_m$  is not similarly clear, because all variables in the (14) are rapidly varying functions of the position of the point. This is why significant variation of the parameters of the system, for example, the magnetic moment of the star, may not lead to significant variation of  $r_m$ . An important quantity is sound speed in the corona, which determines variations of the density and pressure (see section on Initial conditions). Results of our numerical simulations show that it is always a true that  $r_d \approx r_m$ , but in spite of that the matter flow may have different morphology. In a number of cases the magnetic field forms configuration in which some of the poloidal field lines are well-collimated along the symmetry axis, while at larger distances the field

part is pushed toward the equatorial plane (RUKL04). In other cases the collimation along the open field lines is less prominent, but matter flows from the disk along the neutral layer where  $\mathbf{B}_p \approx 0$  (see also RUKL05). We trace such qualitative differences in the final picture of the disk-star interaction to the initial temperature or sound speed in the corona which determines the initial differences of density and pressure.

In the considered model we assume a cold quasi-Keplerian disk surrounded by a relatively hot corona. The disk and corona are in the gravitational field of the central object, a star of mass  $M$  which rotates with angular velocity  $\Omega_*$  around the same axis as the disk. The star has a magnetic moment  $\boldsymbol{\mu}$  which is aligned with the rotational axis of the star.

Having in mind application of the results of the numerical modeling to T Tauri type stars, we mention typical parameters, the mass of the star,  $M = 0.8M_\odot = 1.6 \times 10^{33}\text{g}$ , its radius  $r_* = 2r_\odot = 1.4 \times 10^{11}\text{cm}$ , the inner radius of

the disk,  $r_d = 5r_* = 7 \times 10^{11}$  cm, the magnetic field at the surface of the star (in the equatorial plane),  $B_* = 10^3$  G, the temperature of the corona  $T_{cor} = 10^6$  K, and the temperature of the disk  $T_{disk} = 5 \times 10^3$  K.

The Keplerian velocity at the inner radius of the disk is  $v_K = \sqrt{GM/r_d} \approx 1.2 \times 10^7$  cm/s. The isothermal sound speed in the corona is  $c_{cor} = \sqrt{RT_{cor}/m} \approx 1.3 \times 10^7$  cm/s (for fully ionized hydrogen  $m = 1/2$ ); in the disk  $c_{disk} = \sqrt{RT_{disk}} = 6.5 \times 10^5$  cm/s, where  $R = 8.31 \times 10^7$  ergs/(mol K) is the gaseous constant. The magnetic moment of the star is  $\mu = B_* r_*^3 = 3.43 \times 10^{38}$  G cm<sup>3</sup>. We treat the density in both the disk and the corona as free parameters. For a fixed sound speed in the corona (or the disk) and a given magnetic field of the star, the choice of say the disk density determines the ratio of the Alfvén speed and the sound speed, or equivalently the ratio of the magnetic and gas pressures. We chose the density such that in at least part of corona near the star, the magnetic energy density dominates,  $\mathbf{B}^2/8\pi > \rho v_\phi^2 + p$ . At the inner edge of the disk the Keplerian velocity is related to the sound speed as  $v_K : c_{cor} : c_{disk} \approx 1 : 1 : 0.05$ .

### 3.2. Basic Equations

We assume that the plasma flows are described by the equations of magnetohydrodynamics. Further, we consider that any shock waves in the flow are outside of the considered region, for example, inside the considered region, on the surface of the star. This allows us to use an energy conservation equation in the form of an entropy continuity equation. The system of equations in a non-rotating reference frame is:

$$\begin{aligned}
\frac{\partial \rho}{\partial t} + \nabla \cdot (\rho \mathbf{v}) &= 0, \\
\frac{\partial \rho \mathbf{v}}{\partial t} + \nabla \cdot \mathcal{T} &= \rho \mathbf{g}, \\
\frac{\partial \mathbf{B}}{\partial t} + c \nabla \times \mathbf{E} &= 0, \\
\frac{\partial (\rho S)}{\partial t} + \nabla \cdot (\rho S \mathbf{v}) &= Q.
\end{aligned} \tag{15}$$

Here,  $\rho$  is the density and  $S$  is the specific entropy;  $\mathbf{v}$  is the flow velocity;  $\mathbf{B}$  the magnetic field;  $\mathcal{T}$  the momentum flux-density tensor;  $\mathbf{E}$  the electric field;  $Q$  is the rate of production or loss of entropy per unit volume;  $c$  is speed of light; and  $\mathbf{g} = -(GM/r^2)\hat{\mathbf{r}}$  is the gravitational acceleration due to the star of mass  $M$ . The total mass of the disk is negligible compared to  $M$ .

We consider axisymmetric MHD-flows and use spherical coordinates  $(r, \theta, \phi)$ . The polar angle counted from symmetry axis, all derivatives  $\partial/\partial\phi = 0$ . In spherical co-

ordinates equations (15) have the form:

$$\begin{aligned}
\frac{\partial \rho}{\partial t} + \frac{1}{r^2} \frac{\partial}{\partial r} (r^2 \rho v_r) + \frac{1}{r \sin \theta} \frac{\partial}{\partial \theta} (\sin \theta \rho v_\theta) &= 0, \\
\frac{\partial (\rho v_r)}{\partial t} + \frac{1}{r^2} \frac{\partial}{\partial r} (r^2 \mathcal{T}_{rr}) + \frac{1}{r \sin \theta} \frac{\partial}{\partial \theta} (\sin \theta \mathcal{T}_{r\theta}) &= \\
&= \frac{\mathcal{T}_{\theta\theta} + \mathcal{T}_{\phi\phi}}{r} + \rho g_r, \\
\frac{\partial (\rho v_\phi)}{\partial t} + \frac{1}{r^3} \frac{\partial}{\partial r} (r^3 \mathcal{T}_{r\phi}) + \frac{1}{r \sin^2 \theta} \frac{\partial}{\partial \theta} (\sin^2 \theta \mathcal{T}_{\theta\phi}) &= 0, \\
\frac{\partial (\rho v_\theta)}{\partial t} + \frac{1}{r^3} \frac{\partial}{\partial r} (r^3 \mathcal{T}_{r\theta}) + \frac{1}{r} \frac{\partial}{\partial \theta} \mathcal{T}_{\theta\theta} &= \\
&= \cotan \theta \frac{\mathcal{T}_{\phi\phi} - \mathcal{T}_{\theta\theta}}{r}, \\
\frac{\partial B_r}{\partial t} + \frac{1}{r \sin \theta} \frac{\partial}{\partial \theta} (\sin \theta c E_\phi) &= 0,
\end{aligned}$$

$$\frac{\partial B_\phi}{\partial t} + \frac{1}{r} \frac{\partial}{\partial r} (rc E_\theta) - \frac{1}{r} \frac{\partial}{\partial \theta} (c E_r) = 0,$$

$$\frac{\partial B_\theta}{\partial t} + \frac{1}{r} \frac{\partial}{\partial r} (-c E_\phi) = 0,$$

$$\frac{\partial (\rho S)}{\partial t} + \frac{1}{r^2} \frac{\partial}{\partial r} (r^2 \rho S v_r) + \frac{1}{r \sin \theta} \frac{\partial}{\partial \theta} (\sin \theta \rho S v_\theta) = Q.$$

The stress tensor  $\mathcal{T}$  is

$$\mathcal{T}_{ik} = \rho v_i v_k + p \delta_{ik} + \left( \frac{B^2}{8\pi} \delta_{ik} - \frac{B_i B_k}{4\pi} \right) + \tau_{ik} = T_{ik} + \tau_{ik}.$$

Here,  $p$  is the pressure;  $\tau_{ik}$  is the ‘‘viscous’’ stress caused by the turbulent fluctuations of the velocity and magnetic field;  $g_r = -GM/r^2$  is the acceleration due to gravity. The plasma is considered to be an ideal gas with adiabatic index  $\gamma = 5/3$ , so that  $S = \ln(p/\rho^\gamma)$ .

We assume that the stress due to fluctuations of the velocity and the magnetic field can be represented in the same way as collisional viscosity by substitution of the turbulent viscosity coefficient. Moreover, we consider that the viscous stress is determined mainly by the gradient of the angular velocity because the azimuthal velocity is the dominant component in the disk. The dominant components of the tensor  $\tau_{ik}$  in spherical coordinates are:

$$\tau_{r\phi} = -\nu_t \rho r \sin \theta \frac{\partial \omega}{\partial r},$$

$$\tau_{\theta\phi} = -\nu_t \rho \sin \theta \frac{\partial \omega}{\partial \theta}.$$

Here  $\omega = v_\phi/r \sin \theta$  is angular velocity of the plasma and  $\nu_t$  is the coefficient of the turbulent viscosity.

Separating out the viscous stress gives

$$\frac{\partial(\rho v_\phi)}{\partial t} + \frac{1}{r^3} \frac{\partial(r^3 T_{r\phi})}{\partial r} + \frac{1}{r \sin^2 \theta} \frac{\partial(\sin^2 \theta T_{\theta\phi})}{\partial \theta} = \frac{1}{r^3} \frac{\partial}{\partial r} \left( \nu_t \rho r^4 \sin \theta \frac{\partial \omega}{\partial r} \right) + \frac{1}{r \sin^2 \theta} \frac{\partial}{\partial \theta} \left( \nu_t \rho \sin^3 \theta \frac{\partial \omega}{\partial \theta} \right), \quad (16)$$

where  $T_{r\phi}$  and  $T_{\theta\phi}$  are components of the inviscid part of the stress tensor.

The viscosity leads of course to dissipation of the kinetic energy and its conversion to thermal energy and to a corresponding increase of the entropy. The rate of energy dissipation per unit volume is

$$\frac{\tau_{ik}^2}{2\rho\nu_t} = \frac{\rho\nu_t}{2} \sin^2 \theta \left[ r^2 \left( \frac{\partial \omega}{\partial r} \right)^2 + \left( \frac{\partial \omega}{\partial \theta} \right)^2 \right].$$

We assume that the finite conductivity of plasma as well as “viscous” stresses are connected mainly with the turbulent fluctuations of the velocity and magnetic field. The induction equation averaged over the small-scale fluctuations has the form

$$\frac{\partial \mathbf{B}}{\partial t} - \nabla \times (\mathbf{v} \times \mathbf{B}) + c \nabla \times \mathbf{E}^\dagger = 0. \quad (17)$$

Here,  $\mathbf{v}$  and  $\mathbf{B}$  are the averaged velocity and magnetic fields, and  $\mathbf{E}^\dagger = -\langle (\mathbf{v}' \times \mathbf{B}') \rangle / c$  is electromotive force connected with the fluctuating fields. Because the turbulent electromotive force  $\mathbf{E}^\dagger$  is connected with the small-scale fluctuations, it is reasonable to suppose that it has a simple relation to the ordered magnetic field  $\mathbf{B}$ . If we neglect the magnetic dynamo  $\alpha$ -effect (Moffat 1978), then  $\langle (\mathbf{v}' \times \mathbf{B}') \rangle = -\eta_t \nabla \times \mathbf{B}$ , where  $\eta_t$  is the coefficient of turbulent magnetic diffusivity. Equation (17) now takes the form

$$\frac{\partial \mathbf{B}}{\partial t} - \nabla \times (\mathbf{v} \times \mathbf{B}) + \nabla \times (\eta_t \nabla \times \mathbf{B}) = 0. \quad (18)$$

We should note that the term for  $\mathbf{E}^\dagger$  formally coincides with the Ohm’s law

$$\mathbf{J} = \frac{c}{4\pi} \nabla \times \mathbf{B} = \frac{c^2}{4\pi\eta_t} \mathbf{E}^\dagger.$$

The coefficient of turbulent electric conductivity  $\sigma = c^2/4\pi\eta_t$ . The rate of dissipation of magnetic energy per unit volume is

$$\frac{\mathbf{J}^2}{\sigma} = \frac{\eta_t}{4\pi} (\nabla \times \mathbf{B})^2.$$

To calculate the evolution of the poloidal magnetic field it is useful to calculate the  $\phi$ -component of the vector-potential  $\mathbf{A}$ . Owing to the assumed axisymmetry,

$$B_r = \frac{1}{r \sin \theta} \frac{\partial(\sin \theta A_\phi)}{\partial \theta}, \quad B_\theta = -\frac{1}{r} \frac{\partial(r A_\phi)}{\partial r}.$$

Substituting  $\mathbf{B} = \nabla \times \mathbf{A}$  to the induction equation gives

$$\frac{\partial \mathbf{A}}{\partial t} + c \mathbf{E} = \nabla \chi, \quad (19)$$

where  $\chi$  is an arbitrary function. Thus,

$$\frac{\partial A_\phi}{\partial t} - (\mathbf{v} \times \mathbf{B})_\phi + \eta_t (\nabla \times \mathbf{B})_\phi = 0, \quad (20)$$

or

$$\frac{\partial A_\phi}{\partial t} - \eta_t \left( \frac{1}{r} \frac{\partial^2(r A_\phi)}{\partial r^2} + \frac{1}{r^2} \frac{\partial}{\partial \theta} \frac{1}{\sin \theta} \frac{\partial(\sin \theta A_\phi)}{\partial \theta} \right) = [\mathbf{v} \times \mathbf{B}]_\phi.$$

The azimuthal component of the induction equation gives

$$\begin{aligned} \frac{\partial B_\phi}{\partial t} - \frac{1}{r} \frac{\partial}{\partial r} \left( \eta_t \frac{\partial(r B_\phi)}{\partial r} \right) - \frac{1}{r^2} \frac{\partial}{\partial \theta} \left( \frac{\eta_t}{\sin \theta} \frac{\partial(\sin \theta B_\phi)}{\partial \theta} \right) \\ = \frac{1}{r} \left( \frac{\partial[r(\mathbf{v} \times \mathbf{B})_\theta]}{\partial r} - \frac{\partial(\mathbf{v} \times \mathbf{B})_r}{\partial \theta} \right). \end{aligned} \quad (21)$$

The Joule heating rate per unit volume is

$$\begin{aligned} \frac{\eta_t}{4\pi} (\nabla \times \mathbf{B})^2 = \frac{\eta_t}{4\pi r^2} \times \\ \left[ \left( \frac{\partial(r B_\theta)}{\partial r} - \frac{\partial B_r}{\partial \theta} \right)^2 + \left( \frac{\partial(r B_\phi)}{\partial r} \right)^2 + \frac{1}{\sin^2 \theta} \left( \frac{\partial(\sin \theta B_\phi)}{\partial \theta} \right)^2 \right]. \end{aligned}$$

### 3.3. Initial Data

A variety of simulation runs were calculated for a range of values of the star’s magnetic moment and its angular velocity and for different values of the viscosity and magnetic diffusivity. Changes in the magnetic moment of the star (at  $t = 0$ ) of course changes the location of the surface where  $p + \rho v_\phi^2 = \mathbf{B}^2/8\pi$ .

The initial conditions have a significant role in giving a “smooth” transition of the system to possible stationary, quasi-stationary or a quasi-periodic regime. This role of the initial conditions provides a measure of their validity: the time-averaged location of the Alfvén surface (in the equatorial plane) should not be appreciably different from the its initial value. In the opposite case, a significant part of the computational time can be spent for establishment of more or less equilibrium distribution of the matter and the field.

The initial magnetic field is determined by the magnetic moment of the star. The field is a dipole with field lines connecting the star and the disk. It is clear that the differential rotation of matter along the field lines may lead to the generation of an azimuthal magnetic field and to the opening of some of the field lines (e.g., Lovelace et al. 1995). The qualitative picture of the poloidal field lines is shown in Figure 5. The dashed line shows the line along which the  $r$ -component of magnetic field is zero. A final field configuration could be determined and used as an initial condition. Nevertheless, we have found it efficacious to start with the poloidal dipole field, and let the system evolution open the field lines (see also Romanova et al. 2002).

Initially the matter of the disk and corona are assumed to be in mechanical equilibrium, and the magnetic field is the current-free dipole field of the star  $B_r = 2\mu \cos \theta / r^3$  and  $B_\theta = \mu \sin \theta / r^3$ . In addition, the initial density distribution is taken to be barotropic with

$$\rho(p) = \begin{cases} p/T_{disk}, & p > p_b \quad \text{and} \quad r \sin \theta \geq r_b \\ p/T_{cor}, & p < p_b \quad \text{or} \quad r \sin \theta \leq r_b. \end{cases}$$



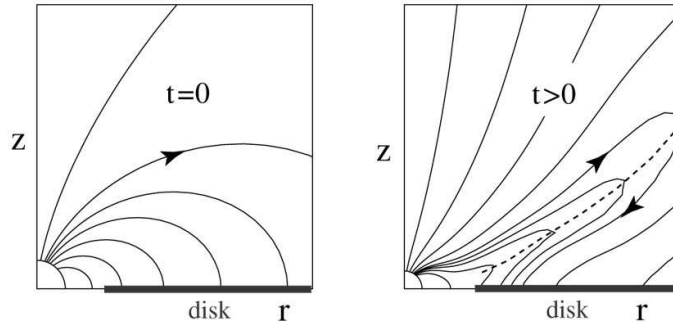


FIG. 5.— Sketches of the initial (left) and final (right) configurations of the poloidal magnetic field which results from the difference in angular velocities of the star and the disk.

The level surface of pressure  $p_b$  separates the cold matter of the disk from the hot matter of corona. At this surface the density has a discontinuity from value  $p_b/T_{disk}$  to value  $p_b/T_{cor}$ .

Because the density distribution is barotropic, the angular velocity is a constant on coaxial cylindrical surfaces about the  $z$ -axis. Consequently, the pressure may be determined from

$$F(p) + \Phi + \Phi_c = E = \text{const} .$$

Here,  $\Phi = -GM/|\mathbf{r}|$  is gravitational potential,  $\Phi_c = \int_{r \sin \theta}^{\infty} \omega^2(\xi) \xi d\xi$  is centrifugal potential, which depends only on cylindrical radius  $r \sin \theta$ , and

$$F(p) = \begin{cases} T_{disk} \ln(p/p_b) , & p > p_b \quad \text{and} \quad r \sin \theta > r_b , \\ T_{cor} \ln(p/p_b) , & p < p_b \quad \text{or} \quad r \sin \theta < r_b . \end{cases}$$

Initially, the inner edge of the disk is located at  $r_b = 5$  in the equatorial plane. The angular velocity of the disk is slightly sub-Keplerian  $\Omega(\theta = \pi/2) = (1 - 0.003)\Omega_K$ , so that the density and pressure decrease towards periphery. Inside the cylinder  $r \leq r_b$  the matter rotates rigidly with the angular velocity  $\Omega(r_b) = (1 - 0.003)\sqrt{GM/r_b^3}$ . To insure the smooth start-up, the angular velocity of the star is changed gradually from its initial value  $\Omega_{cor} = 5^{-3/2} \approx 0.09$  to a final value  $\Omega_*$  during three Keplerian rotation periods at  $r = 1$ .

Below we show results of our simulations for the following set of dimensionless parameters: the gravitational potential is such that  $GM = 1$ ; the dipole moment of the star is  $\mu = 10$ ; the angular velocity of the star is  $\Omega_* = 1$ ; the initial “temperature” of the disk is  $T_{disk} = (p/\rho)_{disk} = 0.0005$ ; the initial temperature of the corona is  $T_{cor} = (p/\rho)_{cor} = 0.5$ . We note that the dimensional temperature is  $T(K) = mv_0^2 T/R$ , where  $v_0$  is the velocity scale,  $m$  is the number of barions per particle (including free electrons), which by itself depends on the temperature, chemical composition and other factors.

#### 3.4. Transition to the Dimensional Variables

Results obtained in dimensionless form may be applied to objects with widely different scales. Below we give examples for classical T Tauri stars (CTTSs) and for neutron stars with a weak magnetic field (millisecond pulsars).

For CTTSs we adopt the following scales. The mass of the star is  $M_0 = M_* = 0.8M_\odot = 1.6 \times 10^{33}$  g. The length scale is  $r_0 = 2r_* = 4r_\odot = 2.8 \times 10^{11}$  cm. The magnetic field at the surface of the star is  $B_* = 10^3$  G. From these numbers we obtain the other scaling variables: The time-scale  $t_0 = 0.166$  days; velocity  $v_0 = 1.95 \times 10^7$  cm/s; density  $\rho_0 = 4.1 \times 10^{-13}$  g/cm<sup>3</sup>; pressure  $p_0 = 156$  erg/cm<sup>3</sup>; accretion rate  $\dot{M}_0 = 6.27 \times 10^{17}$  g/s =  $9.84 \times 10^{-9}$   $M_\odot$ /yr; angular momentum flux  $\dot{L}_0 = 3.43 \times 10^{36}$  gcm<sup>2</sup>/s<sup>2</sup>. For these parameters, the magnetic moment of the star is  $\mu_* = 2.74 \times 10^{36}$  Gcm<sup>3</sup>; the star’s rotation period is  $P_* = 1.04$  days, the initial temperature in the disk is  $T_d = 2,300$  K, and coronal temperature is  $T_c = 1.15 \times 10^6$  K. Subsequently, we give time in periods of rotation of the star.

For a neutron star, we give an illustration of the scales. The star’s mass is  $M_0 = 1.5M_\odot = 3.0 \times 10^{33}$  g. The length scale is  $r_0 = 2r_* = 2 \times 10^6$  cm. The magnetic field at the surface of the star is  $B_* = 10^9$  G. Other scaling variables include the time-scale  $t_0 = 2 \times 10^{-4}$  s, the velocity  $v_0 = 10^{10}$  cm/s, the density  $\rho_0 = 1.56 \times 10^{-6}$  g/cm<sup>3</sup>, the pressure  $p_0 = 1.56 \times 10^{14}$  erg/cm<sup>3</sup>, the accretion rate  $\dot{M}_0 = 6.25 \times 10^{16}$  g/s =  $10^{-9}$   $M_\odot$ /yr, and the angular momentum flux  $\dot{L}_0 = 1.25 \times 10^{33}$  gcm<sup>2</sup>/s<sup>2</sup>. For these parameters, the magnetic moment of the star is  $\mu_* = 10^{27}$  Gcm<sup>3</sup>, the rotation period of the star is  $P_* = 1.26 \times 10^{-3}$  s, the initial temperature in the disk is  $T_d = 3 \times 10^8$  K, and the coronal temperature is  $T_c = 3 \times 10^{11}$  K.

#### 3.5. Numerical Method

For the numerical integration of the MHD equations including magnetic diffusivity and viscosity, we used a method of splitting of the different physical processes. Our simulation algorithm has a number of blocks: (1) a hydrodynamic block in which we calculated the dynamics of the plasma and magnetic field with dissipative processes switched off; (2) a blocks for the diffusion of the poloidal and azimuthal components of the magnetic field calculated for frozen values of the plasma velocity and thermodynamic parameters (density and pressure); and a block for the calculation of viscous dissipation in which we took into account only  $r\phi$  and  $\theta\phi$  components of the viscous stress tensor.

The system of MHD equations (15) was integrated numerically in the region  $r_{int} < r < r_{ext}$ ,  $0 < \theta < \pi/2$ . We

used grids which were equally spaced in  $\theta$ . The steps in the radial direction were chosen so that the poloidal plane cells were curvilinear rectangles with approximately equal sides. A typical region was  $0.5 < r < 50$ ,  $0 < \theta < \pi/2$  with the grid  $85 \times 31$  cells. Figure 6 shows the grid in the entire simulation region (right panel) and in the inner part of the region (left panel).

In the *hydrodynamic* block, the ideal MHD equations are integrated using an explicit Godunov-type numerical scheme. For calculation of fluxes between the cells we used approximate solution of the Riemann problem analogous to one described by Brio & Wu (1988). To guarantee the absence of the magnetic charge, we calculated at each time-step the  $\phi$ -component of the vector-potential  $A_\phi$ . This was then used to obtain the poloidal components of the magnetic field ( $B_r, B_\theta$ ) in divergence-free form (Toth 2000).

In the block where the *diffusion* of the poloidal magnetic field is calculated, we numerically integrated the equation (20) for the  $\phi$ -component of vector-potential. During this calculation we frozen the values of  $A_\phi$  on the inner and outer boundaries of the simulation region. In the equatorial plane we have conditions of symmetry,  $\partial A_\phi / \partial \theta = 0$ . On the symmetry axis we have  $A_\phi = 0$ .

Equation (20) was approximated with an implicit difference scheme. The approximation was chosen so that the operator on the implicit time-layer was symmetric and positive.

For solving the system of equations on the implicit time-layer, we used ICCG method (Incomplete Cholesky Conjugate Gradient method). Because the size of the grid cells and values of the coefficient of the magnetic diffusivity vary strongly in space, the elements of the matrix of the system also vary strongly. To remove this undesirable property, we changed the matrix so that it has diagonal elements equal to unity.

In the block where the diffusion of the azimuthal component of the magnetic field was calculated, we numerically integrated equation (21). At the inner and outer boundaries the  $B_\phi$  was frozen at this computational block. Along the rotation axis and on the equatorial plane  $B_\phi = 0$ .

Equation (21) was approximated by a numerical scheme with symmetric and positive operator on the implicit time layer. The corresponding system of linear equation was solved by the ICCG-method with pre-conditioning.

In the block of our code where the *viscous* stress is calculated, we numerically integrated the equation (16) for the angular velocity of matter  $\omega = v_\phi / r \sin \theta$ . At the inner boundary of the simulation region we take  $\omega = \Omega_*$ , the angular rotation velocity of the star. At the outer boundary,  $\omega$  is taken to be fixed and equal to the corresponding Keplerian value. On the axis and in the equatorial plane we have the condition of zero stress for the  $\theta\phi$ -component of the viscous stress tensor.

Equation (16) was approximated by a numerical scheme with the symmetric and positive operator on the implicit time-layer. The corresponding system of linear equations was solved by the ICCG-method with pre-conditioning.

#### 4. RESULTS

We performed simulations of accretion to a star in the “propeller” regime for a wide range of parameters,  $\mu$ ,  $\Omega_*$ ,

$\alpha_v$  and  $\alpha_d$ . In the following we discuss results for the reference case  $\mu = 10$ ,  $\Omega_* = 1$ ,  $\alpha_v = 0.2$ , and  $\alpha_d = 0.2$ .

The reference case was calculated out to a time corresponding to 2500 rotation periods of the star. We observed that the process of interaction between the magnetosphere and the disk is accompanied with (1) oscillations of the disk, (2) quasi-periodic opening and closing of the magnetic field, (3) quasi-periodic outbursts to winds and jets. This evolution arises from the diffusive mixing of the disk matter with the magnetic field of the star, the opening of the magnetic field lines linking the star and disk, unloading of the disk matter to the star and to the outflows, and the outflow of angular momentum from the star and from the disk.

The left-hand panel of Figure 7 shows the variation of the inner radius of the disk which was calculated at the density level,  $\rho_0 = 0.3$ . Note that near the disk-corona boundary,  $\rho(r, \theta, t) = \rho_0$ , the density gradient is very large so that the choice of  $\rho_0$  is not important. During an initial time  $t \sim 100$ , part of the magnetic flux outgoing the star opens and subsequently varies about an average value. To determine this magnetic flux we calculated the dependence of the maximum value of the magnetic flux function  $\Psi(r, \theta, t) = r \sin \theta A_\phi$ ,  $\Psi_0 = \max_\theta \Psi(r_0, \theta, t)$  on time at the sphere of radius  $r_0 = 30$ . The magnetic field lines along which  $\Psi > \Psi_0$ , are evidently closing inside the sphere of radius  $r_0$ . The value  $\Psi_0$  determines the location of the last closed field line at this distance, in particular the radius at which this field line crosses equatorial plane  $r_{eq} = \mu / \Psi_0(t)$ . That is,  $r_{eq}$  shows the radius of the closed magnetosphere. The right-hand panel of Figure 7 shows that this radius  $r_{eq}(t)$  varies with time in a fashion similar to  $r_d(t)$ ; however, the amplitude is much smaller.

An important aspect of the interaction between a rapidly rotating magnetized star and an accretion disk is the transport of angular momentum. The equation for the conservation of angular momentum can be obtained from (16) by multiplying it by  $r \sin \theta$ ,

$$\frac{\partial(\rho v_\phi r \sin \theta)}{\partial t} + \frac{1}{r^2} \frac{\partial}{\partial r} \left\{ r^2 \left[ r \sin \theta \left( T_{r\phi} - \nu_t \rho r \sin \theta \frac{\partial \omega}{\partial r} \right) \right] \right\} + \frac{1}{r \sin \theta} \frac{\partial}{\partial \theta} \left\{ \sin \theta \left[ r \sin \theta \left( T_{\theta\phi} - \nu_t \rho \sin \theta \frac{\partial \omega}{\partial \theta} \right) \right] \right\} = 0,$$

where  $T_{r\phi} = \rho v_r v_\phi - B_r B_\phi / 4\pi$  and  $T_{\theta\phi} = \rho v_\theta v_\phi - B_\theta B_\phi / 4\pi$  are the components of “non-viscous” part of the stress tensor.

The angular momentum conservation equation evidently has the form of a continuity equation,

$$\frac{\partial(\rho \ell)}{\partial t} + \nabla \cdot \mathbf{L} = 0,$$

where  $\ell = v_\phi r \sin \theta$  is the specific angular momentum and the angular momentum flux density is

$$\mathbf{L} = r \sin \theta \left( \rho v_\phi \mathbf{v}_p - \frac{B_\phi \mathbf{B}_p}{4\pi} - \nu_t \rho r \sin \theta \nabla \omega \right).$$

The first term on the right-hand-side  $\mathbf{L}$  gives the transport of angular momentum by the matter; the second term is magnetic field contribution; and the third term is the transport due to viscous stress.

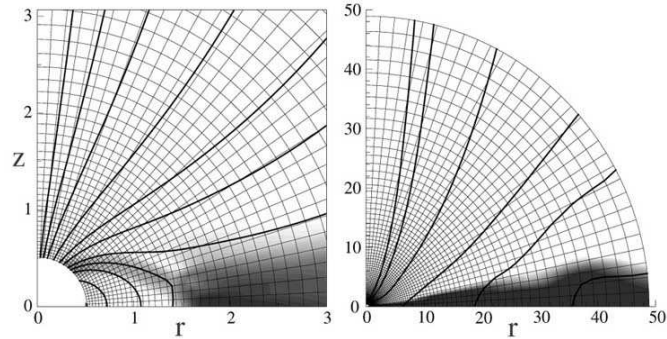


FIG. 6.— The left-hand panel shows the inner part of the simulation region with the logarithm of density as a background and the magnetic field lines (solid lines) and the grid. The right-hand panel shows the full simulation region.

Figure 8 (a,b,e-g) shows the angular momentum fluxes at  $t = 2300$ . The streamlines show the direction of the fluxes, while the background shows the magnitude of the flux. Figures 8 (a, e) show the distribution of the angular momentum fluxes carried by the magnetic field at large and small scales.

Figures 8(b, f) show the corresponding fluxes carried by the matter. From Figure 8e it is clear that the angular momentum outflow from the star is due mainly to the twisting of the magnetic field. Note that a larger part of angular momentum is carried along the open field lines. Other part of angular momentum which is along the closed field lines is transported from the star to the disk. Angular momentum carried by matter is largest in the disk and in the conical outflow in the vicinity of the neutral layer (Fig. 8b). Here magnetic pressure is not very high, while pressure and density of matter play larger role. Bottom panels show energy fluxes carried by the magnetic field (Fig. 8c) and by matter (Fig. 8d). One can see from Figure 8c that significant energy is carried from the star by a Poynting flux.

Figure 8g shows the angular momentum flux carried by the viscous stress. This stress is large at the boundary between the disk and magnetosphere in the vicinity of the equatorial plane. This is the place of significant gradients of the angular velocity of matter, as one can see from the Figure 9 (shown at the same time  $t = 2300$ ). This figure also shows the distribution of density, entropy (logarithm scale at the right), and radial velocity  $v_r$  in the equatorial plane. It is evident that the disk has a sharp boundary

both in density and in entropy.

Next, we evaluate the directions where most of the matter and angular momentum outflows. For this we calculated the distribution of the fluxes of matter and angular momentum as a function of  $\theta$  (the colatitude) as a function of time at a given distance  $r_0 = 20$ . Figure 10 shows a plot of these distributions as a function of time. One can see that the matter flux to the wind is mainly in the range  $40^\circ < \theta < 70^\circ$ . Thus, most of the matter flows into a wide-angle hollow-cone with a large inclination angle to the  $z$ -axis (Figure 10a). There is also a flux of matter towards the star which is associated with the equatorial region of the disk. The angular momentum flux carried by matter has distribution similar to the distribution of the matter flux (see Figure 10b). The angular momentum flux carried by the magnetic field (Figure 10c) is concentrated in two stripes:  $0^\circ < \theta < 30^\circ$  (near the axis), and  $60^\circ < \theta < 80^\circ$  (closer to the disk). The larger flux is associated with the angular momentum outflow in collimated jet, along the field lines which start at the surface of the star. The other stripe, at larger angles  $\theta$  is connected with the disk wind.

The wide-angle, hollow-cone disk wind is similar to the stationary magnetocentrifugally driven winds predicted by Blandford and Payne (1982) and Lovelace, Berk, and Contopoulos (1991) and first obtained and analyzed in MHD simulations by Ustyugova et al. (1999). For such winds the angle of the poloidal field to the  $z$ -axis at the surface of the disk  $\Theta = \tan^{-1}(|B_r/B_z|)$  is predicted to be  $\gtrsim 30^\circ$ . On the other hand a magnetically dominated (or

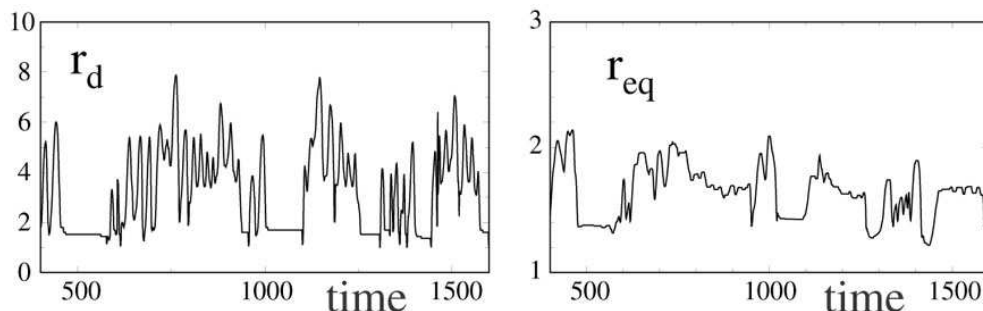


FIG. 7.— The left-hand panel shows the variations of the inner radius of the disk. The right-hand panel shows the variations of the radius where a given magnetic field line crosses the equatorial plane.

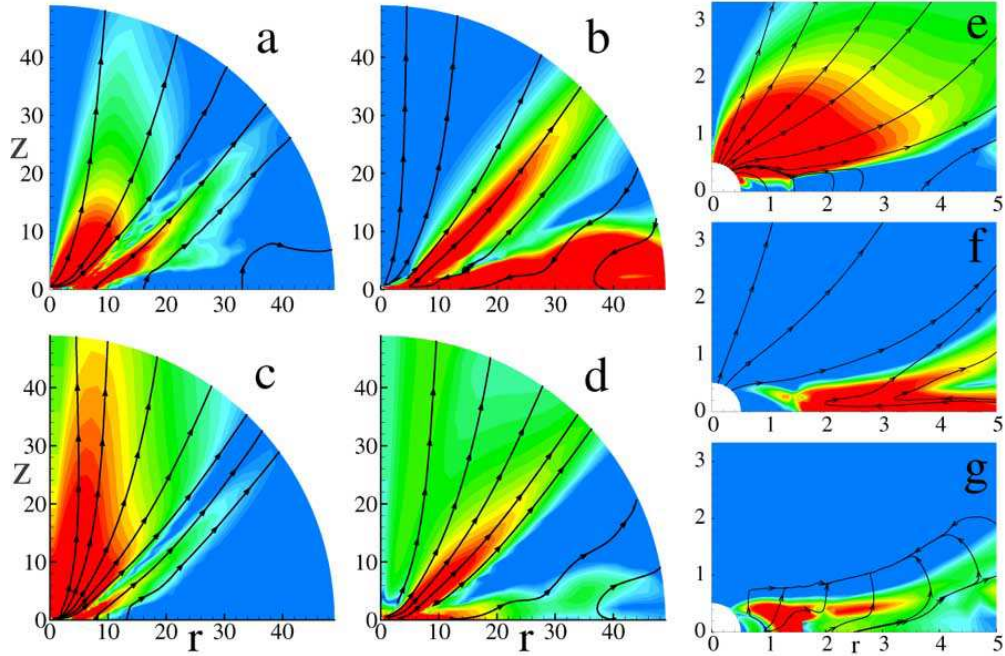


FIG. 8.— The top panels show the angular momentum flux carried by the field (a) and by the matter (b). The bottom panels show the energy fluxes carried by the field (c) and by the matter (d). The right-hand panels show the angular momentum fluxes close to the star carried by the field (e), by the matter (f), and by the viscous stress (g). The background color indicates the value of the flux while the streamlines indicate the direction of the flux.

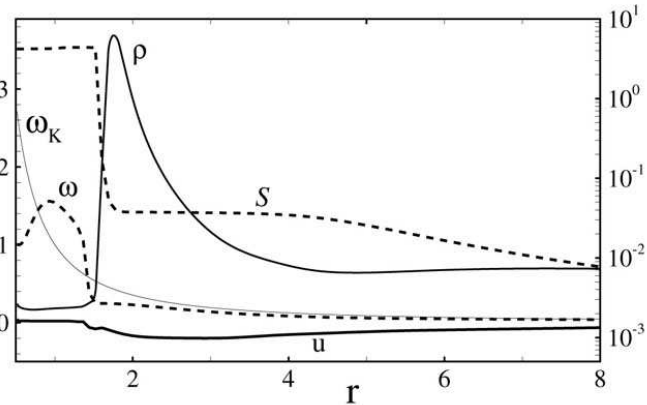


FIG. 9.— Radial distribution of different variables in the equatorial plane, the density  $\rho$ , the specific entropy  $S$ , the radial velocity  $v_r$ , the angular rotation rate  $\omega = v_\phi/r$ , and the Keplerian angular velocity  $\omega_K$ . The scale for the entropy is on the right-hand side.

Poynting) outflow from a disk or star can have the angle  $\Theta$  less than  $30^\circ$  (Ustyugova et al. 2000; Lovelace et al. 2002). The narrow-angle, hollow-cone jet along the open field lines of the star has much smaller values of  $\Theta$  and it is magnetically dominated.

Figure 11 shows the distribution of different physical quantities in the computational region (top panels) and on a smaller scale (bottom panels). Figures 11 (a, d) show distribution of the matter flux  $\rho v_p$ , and streamlines of matter flow at time  $t = 2300$ . One can see that matter flows with the disk, then turns near the magnetosphere of the star and flows outward in a disk wind. Some matter goes around the magnetosphere and flows to the jet along the field lines starting at the stellar surface. The white line

shows the escape velocity  $v_{esc} = \sqrt{2GM/r}$ . Above this line  $v > v_{esc}$ . The color background of Figures 11 (b, e) shows the plasma  $\beta \equiv 8\pi p/B^2$  parameter. The dashed white line corresponds to  $\beta = 1$ . Figures 11 (c, f) show isocontours of the  $r \sin\theta B_\phi$  which is the poloidal current flow through a horizontal disk  $\leq r \sin\theta$  centered on the  $z$ -axis.

Figure 12 shows plots of different variables as a function of distance along a magnetic field line which starts from the disk in the vicinity of the neutral field line where the matter flux to the wind is the largest. The solid line shows the projection of the poloidal velocity onto this field line, the dashed line shows the projection of the velocity component normal to the magnetic field line. One can

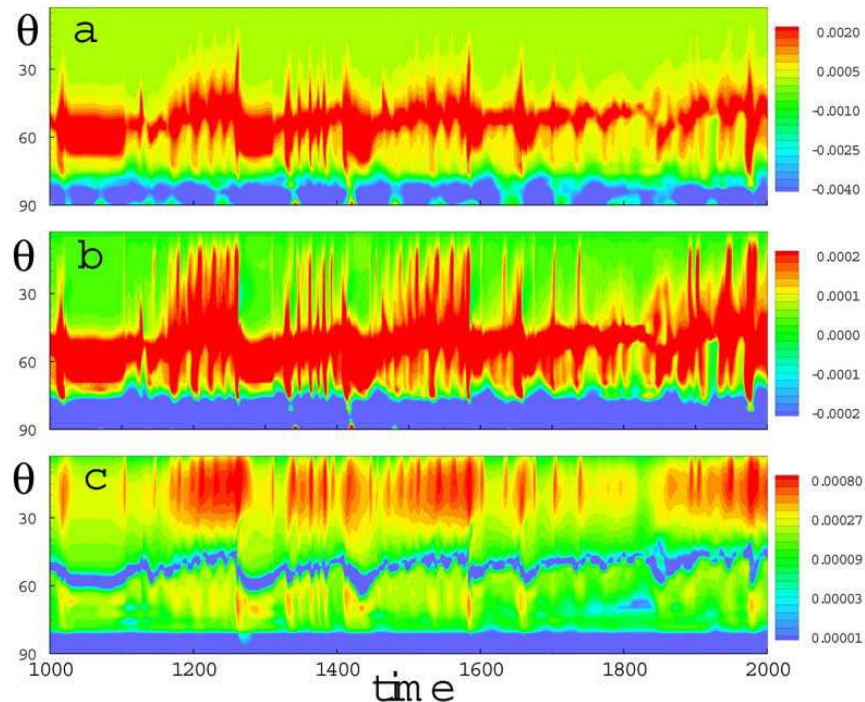


FIG. 10.— Angular ( $\theta$ ) distributions of different fluxes on the surface of a sphere of radius  $r_0 = 20$  as a function of time: (a) shows the matter flux; and (b) and (c) show the radial angular momentum flux carried by the matter and by the magnetic field, respectively.

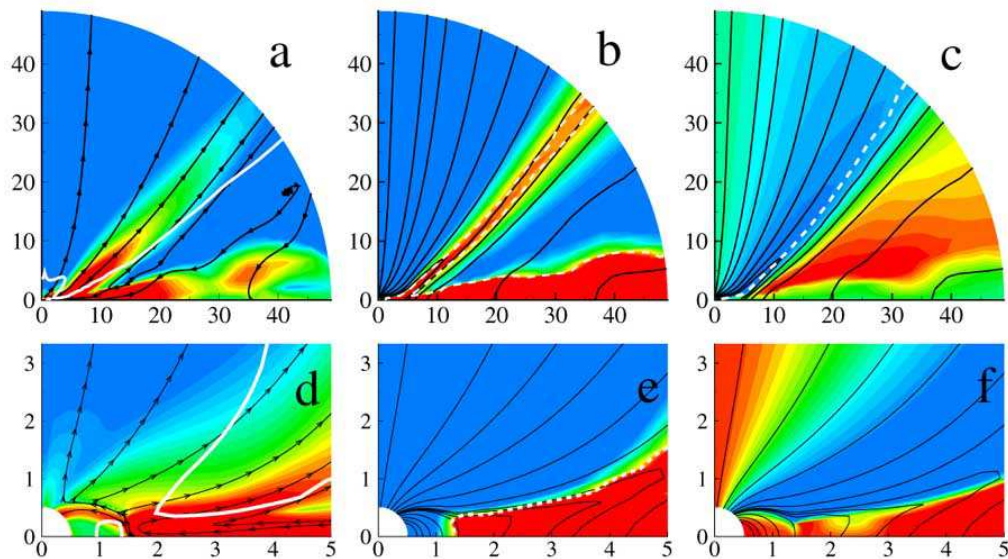


FIG. 11.— In panel (a) the background shows the matter flux and the lines are the streamlines of the matter flow. The white line is the  $v = v_{esc}$  line. In panel (b) the background shows the plasma parameter  $\beta = 8\pi p/B^2$ . The streamlines are the magnetic field lines, and the white dashed line shows the  $\beta = 1$  line. In panel (c) the background shows  $r \sin \theta B_\phi$ , which for steady conditions is the total poloidal current through a disk  $\leq r \sin \theta$  center on the  $z$ -axis. The lines are the magnetic field lines. The white dashed line shows the neutral line where  $B_p = 0$ . The bottom panels (d - f) show the same as (a - c) but in the vicinity of the star.

see that the poloidal velocity is nearly parallel with the poloidal field, which is in accord with the theory of stationary axisymmetric flows of ideally conducting plasma (see, e.g., Ustyugova et al. 1999). The sound speed  $c_s$  and escape velocity  $v_{esc}$  are also shown. One can see that the

flow becomes supersonic and that the flow velocity exceeds the escape velocity  $v_{esc}$ . Earlier, Ustyugova et al. (1999) obtained dependences similar to those of Figure 12 for the case of an ordered magnetic field threading a disk around a non-magnetized star.

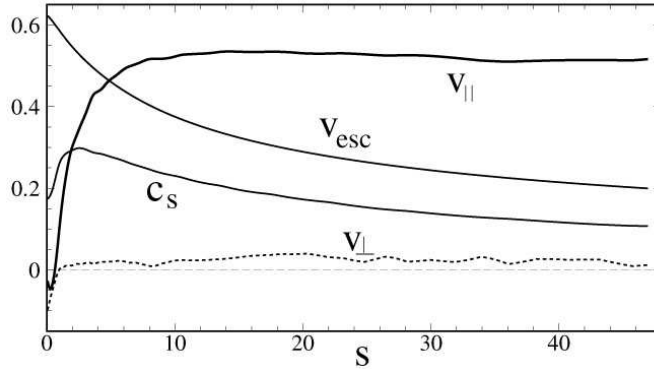


FIG. 12.— Velocities along a field line which starts from the disk near the neutral line of the magnetic field (where the matter flux to the wind is the largest).  $v_{\parallel}$  is the velocity component parallel to the field line and  $v_{\perp}$  is the component perpendicular to the field line.  $v_{esc}$  is escape velocity and  $c_s$  is a sound speed.

Interaction of the magnetized star with the accretion disk can lead to the outflow and escape of a significant fraction of the matter incoming in the disk. We find in general that there is a *jet* and a *disk wind* giving outflows of energy, angular momentum, and matter from the system. The *jet* is identified as the flow in the region within the neutral line of the poloidal magnetic field. The magnetic flux in the jet is the flux emanating from the star. The *disk wind* is the flow outside of the neutral line of the poloidal magnetic field. For both outflows we take into account only the matter which has a velocity higher than the escape velocity  $v_{esc}$ .

Thus, the simulation region includes three flow regions, the disk, the jet, and the wind. These regions do not constitute the entire simulation volume because part of it is filled with relatively rarefied matter of magnetosphere and corona. Accreting matter which is not accelerated to escape speed goes into the magnetosphere or the corona. These regions do not have a significant role in the matter and angular momentum flow. The star has an important role in absorbing mass and losing angular momentum. The star influences the plasma dynamics through the inner boundary of the simulation region. However the influence of the plasma on the star is noticeable on only an extremely long time scale. Figure 13 shows the interactions between the different elements of the system. Evidently, matter which comes through an accretion disk flows in part to the disk wind, in part to the jet, and in part accretes to the star. There is also angular momentum transport between different elements. The star represents a large reservoir of angular momentum which is transported to the disk through the closed field lines and to the jet through the open field lines. The positive direction of the fluxes is shown by arrows.

In all cases the fluxes of matter and angular momentum oscillate strongly in time, but always vary around an average value. See for example Figure 10. For this reason we calculated the time-averaged fluxes and investigated their dependences on the parameters of the model. We took as a base the mentioned reference case with dimensionless parameters  $\mu = 10$ ,  $\Omega_* = 1$ ,  $\alpha_v = 0.2$ , and  $\alpha_d = 0.2$ . A series of simulations was then done to obtain the dependences of the time-averaged fluxes on different parameters. Only one parameter was varied in each series. Figures 14-16

show the derived dependences.

Figure 14 (a-d) show the dependences of the matter fluxes on our main parameters. Here,  $\dot{M}_d$  is the mass accretion rate in the disk at the radius  $r_0 = 30$ ,  $\dot{M}_s$  is the accretion rate to the star,  $\dot{M}_w$  is the matter flux to the wind,  $\dot{M}_j$  is the matter flux to the jet. As we mentioned, we distinguish between “strong” (with outflows) and “weak” (no outflows) propellers. Results of modeling of the “strong” propellers are marked with the filled symbols, while the “weak” propeller results are indicated by open symbols. Different symbols show different dependences:  $\dot{M}_j$  (squares),  $\dot{M}_w$  (circles),  $\dot{M}_d$  (triangles), and  $\dot{M}_s$  (gradient signs). The solid lines show approximations of these dependences. Most of dependences could be approximated by a simple power law and have a clear sense. For example, the larger the magnetic moment  $\mu$  and the larger the angular velocity of the star  $\Omega_*$ , the larger matter fluxes to the wind and jet and the smaller the accretion rate to the star. At smaller  $\mu$  and  $\Omega_*$ , ejection of matter to the wind and jet becomes less efficient and we enter the “weak” propeller regime with very weak or no outflows (see Fig. 14 a,b). Note, that all “weak” propellers are on the left-hand side of the plots.

It is interesting to look at dependences on viscosity,  $\alpha_v$  (see Fig. 14c). We see that matter fluxes to the wind/jet strongly increase with increase of viscosity, while the accretion rate to the star decreases. We conclude that the viscous stress contributes to launching the outflows. At sufficiently small viscosity,  $\alpha_v \lesssim 0.1$ , outflows are absent. The role of the viscosity is twofold. From one side, at larger viscosity, the “friction” between the inner regions of the disk and magnetosphere is larger. From other side, the radial velocity in the disk is proportional to  $\alpha_v$ , so that viscosity increases the matter flux per unit area and the inner region of the disk come closer to the inner regions of the fast rotating magnetosphere. Both factors lead to enhanced outflows, but it is difficult to separate the two factors. In RUKL05 test simulations were done for a case with  $\alpha_v = 0.1$ , and with the density in the disk doubled. This of course increased the accretion rate but it also enhanced the outflows.

Figure 14d shows the dependence on the magnetic diffusivity. The dependence of the matter fluxes to the

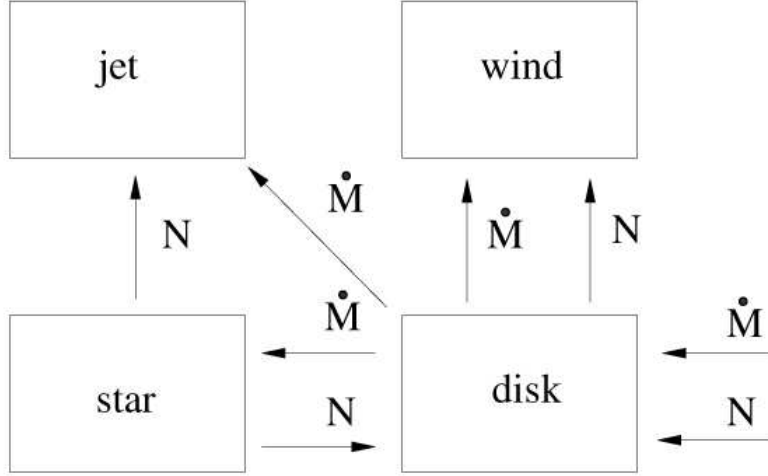


FIG. 13.— Scheme of interaction between different elements of the system.

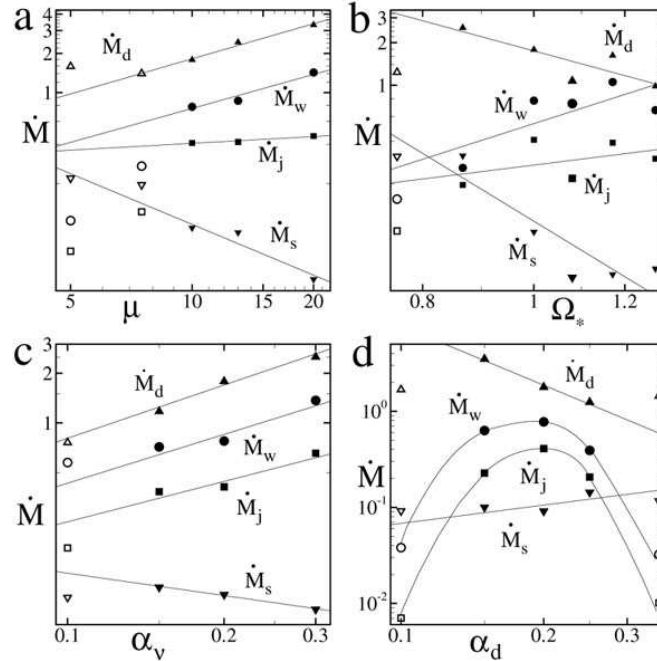


FIG. 14.— Variation of the matter fluxes as a function of different parameters.

wind/jet on  $\alpha_d$  is more complicated than other dependences. Namely, for  $\alpha_d \lesssim 0.2$ , the fluxes  $\dot{M}_w$  and  $\dot{M}_j$  decrease with  $\alpha_d$ , because the mixing of the disk matter with the magnetic field of the magnetosphere become less and less efficient, and correspondingly the angular momentum transport from the star to the disk matter decreases. On the other hand, for  $\alpha_d \gtrsim 0.2$ , the diffusivity become too high, and the inner regions of the disk and magnetosphere are not coupled sufficiently to transport angular momentum. This explains the parabolic approximations of these dependences. We took into account all dependences shown in Figures 14 (a-d), and approximated them with analytic functions. We approximated the dependences on  $\alpha_d$  with power laws to the left and to the right of the dividing value  $\alpha_d \approx 0.2$ . In Figures 14 (c-d), we show the dependences around  $\alpha_v \sim 0.2$  and  $\alpha_d \sim 0.2$ . We have made additional

runs not shown in the plot at much smaller  $\alpha_v$  and  $\alpha_d$ , down to 0.01. Also we have made runs for much larger values, up to 0.6. We show below dependences which incorporated all these runs, separately, for  $\alpha_d > 0.2$  and  $\alpha_d < 0.2$ . The matter fluxes to the wind  $\dot{M}_w$ , to the jet  $\dot{M}_j$ , through the disk  $\dot{M}_d$ , and to the star  $\dot{M}_s$  were approximated as:

$$\dot{M}_w = 0.8\Omega_*^{2.6} \left(\frac{\mu}{10}\right)^{0.9} \left(\frac{\alpha_v}{0.2}\right) \begin{cases} \left(\frac{\alpha_d}{0.2}\right)^{-4.4} & \alpha_d > 0.2 \\ \left(\frac{\alpha_d}{0.2}\right)^2 & \alpha_d < 0.2 \end{cases},$$

$$\dot{M}_j = 0.4\Omega_* \left(\frac{\mu}{10}\right)^{0.2} \left(\frac{\alpha_v}{0.2}\right)^{0.8} \begin{cases} \left(\frac{\alpha_d}{0.2}\right)^{-3.6} & \alpha_d > 0.2 \\ \left(\frac{\alpha_d}{0.2}\right)^{1.7} & \alpha_d < 0.2 \end{cases},$$

$$\begin{aligned}\dot{M}_s &= 0.1\Omega_*^{-5} \left(\frac{\mu}{10}\right)^{-1.3} \left(\frac{\alpha_v}{0.2}\right)^{-0.5} \left(\frac{\alpha_d}{0.2}\right)^{0.6}, \\ \dot{M}_d &= 1.8\Omega_*^{-2.2} \left(\frac{\mu}{10}\right)^{0.9} \left(\frac{\alpha_v}{0.2}\right) \left(\frac{\alpha_d}{0.2}\right)^{-2.1}.\end{aligned}$$

The matter flux to the disk wind increases with  $\mu$  almost linearly and strongly increases with  $\Omega_*$ , while the accretion rate to the star  $\dot{M}_s$  strongly decreases. We note that dependences on  $\mu$  and  $\Omega_*$  have a threshold character. Namely, the matter fluxes to the wind and to the jet strongly decrease for  $\mu \lesssim 7$  and  $\Omega_* \lesssim 0.8$ , where the system enters the “weak” propeller regime (see open symbols in Figures 14 a,b). One can see from the Figure 14b that the dependence of  $\dot{M}_w$  and  $\dot{M}_j$  on the angular velocity of the star  $\Omega_*$  also has a threshold behavior for  $\Omega_* \lesssim 0.8$ . These threshold dependences reflect the qualitative difference between “strong” propellers (with outflows) and “weak” propellers (with no outflows).

As a measure of the efficiency of the propeller interaction with the disk, we take the ratio of the outflow rate to the disk wind and jet to the accretion rate through the disk,  $\mathcal{S} = \dot{M}_{jw}/\dot{M}_d$ . For the larger values of  $\mathcal{S}$ , less matter reaches the surface of the star. Correspondingly, a larger part of the disk matter acquires additional angular momentum and flows to the jet and/or wind. Figures 15 a-d show the dependences of the value  $\mathcal{S}$  on the parameters of the model. The efficiency of the propeller depends weakly on the magnetic moment of the star. The larger the angular velocity of the star and the larger the  $\alpha$ -coefficient of viscosity, the higher is the efficiency of the propeller. The dependence of the efficiency on the  $\alpha$ -coefficient of magnetic diffusivity has a maximum near  $\alpha_d \sim 0.2$ . We found the following dependences,

$$\frac{\dot{M}_{jw}}{\dot{M}_d} = 0.7\Omega_*^{5.6} \left(\frac{\mu}{10}\right)^{-0.2} \left(\frac{\alpha_v}{0.2}\right)^{1.3} \begin{cases} \left(\frac{\alpha_d}{0.2}\right)^{-4.7} & \alpha_d > 0.2 \\ \left(\frac{\alpha_d}{0.2}\right)^{1.7} & \alpha_d < 0.2 \end{cases}.$$

Another measure of the efficiency of the propeller is the ratio of the total matter flux going to the wind/jet to the matter flux to the star,

$$\frac{\dot{M}_{jw}}{\dot{M}_s} = 13\Omega_*^{10} \left(\frac{\mu}{10}\right)^2 \left(\frac{\alpha_v}{0.2}\right)^{2.5} \begin{cases} \left(\frac{\alpha_d}{0.2}\right)^{-3.9} & \alpha_d > 0.2 \\ \left(\frac{\alpha_d}{0.2}\right)^{2.1} & \alpha_d < 0.2 \end{cases}.$$

The ratio of outflow to accretion increases strongly with  $\mu$  and  $\Omega_*$ .

Next, we discuss angular momentum transport from the star and its dependence on main parameters of the model. The outflow of angular momentum from the star causes it to spin down. Part of the angular momentum is carried by the matter, another part by the tension of the magnetic field lines, and a further part by the viscous stress.

The flux of angular momentum from the star was calculated as

$$N_s = \int d\mathbf{S} \cdot r \sin \theta \left[ \rho v_\phi \mathbf{v}_p - \frac{B_\phi \mathbf{B}_p}{4\pi} - \nu_t \rho r \sin \theta \nabla \omega \right],$$

where the integration was over the surface of the inner boundary of the simulation region which is close to the

surface of the star and where  $d\mathbf{S}$  is the surface element directed outward to the region. Simulations show that close to the star angular momentum flux is determined mainly by the magnetic stress.

Part of the flux is associated with the closed field lines. These are field lines connecting a star and the disk. Other part is associated with the open field lines, which connect a star with the low-density corona. We calculated a total flux  $N_s$  and also a flux associated with the closed field lines,  $N_{sd}$ , that is angular momentum flux transported from the star to the disk.

Figure 16 shows fluxes  $N_s$  (gradient signs) and  $N_{sd}$  (circles). We found the following dependences on different parameters:

$$\begin{aligned}N_{sd} &= 1.5\Omega_*^{1.5} \left(\frac{\mu}{10}\right)^{1.2} \left(\frac{\alpha_v}{0.2}\right)^{0.3} \begin{cases} \left(\frac{\alpha_d}{0.2}\right)^{-0.2} & \alpha_d > 0.2 \\ \left(\frac{\alpha_d}{0.2}\right)^{0.14} & \alpha_d < 0.2 \end{cases}, \\ N_s &= 3.1\Omega_*^2 \left(\frac{\mu}{10}\right)^{1.1} \left(\frac{\alpha_v}{0.2}\right)^{0.1} \begin{cases} \left(\frac{\alpha_d}{0.2}\right)^{-0.4} & \alpha_d > 0.2 \\ \left(\frac{\alpha_d}{0.2}\right)^{0.5} & \alpha_d < 0.2 \end{cases}.\end{aligned}$$

Figure 16 (a, b) shows that both fluxes increase with  $\mu$  and  $\Omega_*$ . They increase with a similar rate so that the lines in Figures 16 (a,b) are almost parallel. Figures 16 (c,d) show that the fluxes depend only weakly on the  $\alpha$  coefficients of viscosity and diffusivity. They have maximum at  $\alpha_d \sim 0.2$ . Note that the angular momentum flux carried by the open field lines of the jet  $N_s - N_{sd}$  is similar to that carried by the closed field lines. That is, a star in the propeller regime in our range of parameters spins-down due to both: open and closed field lines.

Now, we can estimate the time-scale of spin-down for CTTSs and accreting neutron stars for parameters given in §3.4. For CTTSs, the loss of the angular momentum of the star in our main case is  $N_s = 3.1\dot{L}_0 = 1.06 \times 10^{37} \text{gcm}^2/\text{s}^2$ . The star’s angular velocity is  $\Omega = 2\pi/P \approx 7 \times 10^{-5} \text{s}^{-1}$ , its angular momentum is  $J = kMr^2\Omega = 2.2 \times 10^{51} k \text{gcm}^2/\text{s}$ , where  $k < 1$ . Taking  $k = 0.4$ , the spin-down time-scale is  $\tau = J/N_s \approx 2.7 \times 10^6$  years. Note, that this time-scale was calculated for a magnetic field  $B_* = 10^3 \text{G}$  and a relatively low accretion rate,  $\dot{M} \approx 10^{-8} M_\odot/\text{yr}$ . The time-scale decreases with magnetic field of the star as  $\sim B^{-1.1}$  and will be  $\tau \approx 8.1 \times 10^5$  years for  $B_* = 3 \times 10^3 \text{G}$ . Time-scale also decreases with matter flux. Thus, if CTTSs have a strong magnetic field in the past, then they were at the propeller regime and were spun-down in  $< 10^6$  years. This time-scale is shorter than typical life-time of the CTTSs, which is  $\sim 10^7 - 10^8$  years. We conclude that propeller mechanism may be responsible for fast spinning-down of CTTSs to presently observed slow rotation in the early stages of their evolution.

For an accreting neutron star,  $N_s = 3.1\dot{L}_0 = 3.87 \times 10^{33} \text{gcm}^2/\text{s}^2$ ,  $\Omega = 2\pi/P \approx 5 \times 10^3 \text{s}^{-1}$ . The star’s angular momentum is  $J = kMr^2\Omega = 1.5 \times 10^{49} k \text{gcm}^2/\text{s}$ . The time-scale of spin-down is  $\tau = J/N_s \approx 2.5 \times 10^7$  years. This time-scale is shorter than expected life-time of millisecond pulsars in the accreting stage. However, millisecond pulsars have a different history of evolution compared



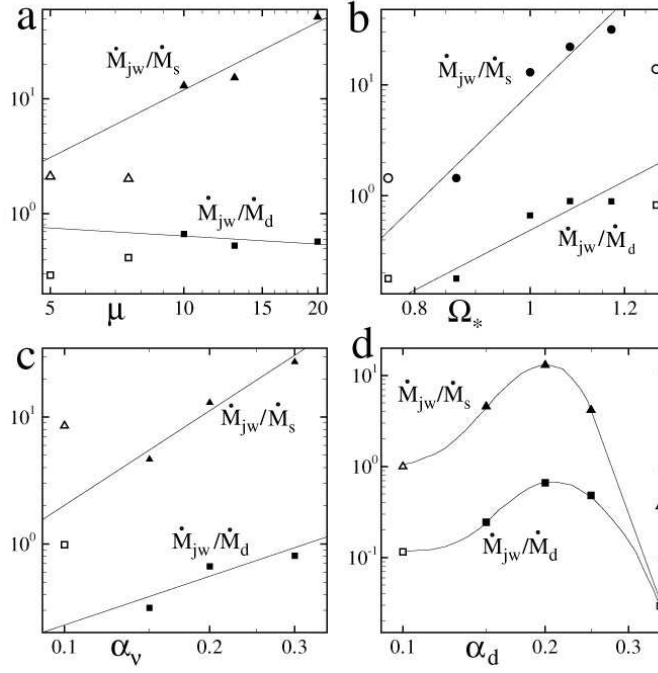


FIG. 15.— Efficiency of the propeller as a function of different parameters as discussed in the text.

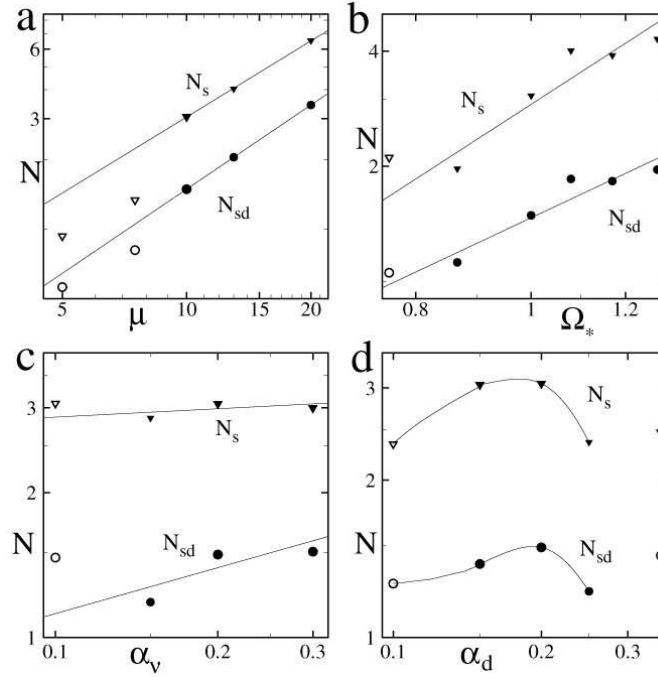


FIG. 16.— Variation of the angular momentum fluxes with parameters of the system .

to CTTs, and they expected to be spined up during accreting stage (Bisnovatyi-Kogan & Komberg 1974). However, the pulsar mechanism may be responsible for fast spinning-down of the pulsar during periods of decreased accretion rate.

## 5. CONCLUSIONS

We performed a large number of axisymmetric MHD simulations and did extensive analysis of the interaction of

a rapidly rotating magnetized star with an accretion disk in the propeller regime. The results can be divided to two classes, “strong” propellers and “weak” propellers. The “strong” propeller is characterized by the intense, wide-angle, conical matter outflow in the vicinity of the neutral line of the poloidal magnetic field and formation of well collimated, magnetically dominated jets along the rotational axis. In the “weak” propeller regime there are no appreciable matter outflows from the disk and the collimated

flow along the axis is much weaker.

In this work the four main parameters of the model were varied: the magnetic moment of the star, its angular velocity, and  $\alpha$ -coefficients of the kinematic viscosity and magnetic diffusivity. We calculated time-averaged total fluxes of matter, energy, and angular momentum and investigated their dependences on the main parameters of the model. The average characteristics were calculated during 1000 – 2500 periods of rotation of the inner disk. The derived dependences were approximated in most cases by power law functions. But some dependences showed a threshold character with the flux becoming negligible for a range of the parameters.

In all cases the interaction of the magnetized star with the accretion disk showed strongly non-stationary, quasi-periodic character. For example, in the reference case described in the paper, the typical “period” of oscillations is

several tens of our time-units. All fluxes of matter, energy, and angular momentum to the wind, jet, and star oscillate strongly with time.

Our simulation results are applied to classical T Tauri stars and to millisecond pulsars. We conclude that propeller mechanism may be responsible for fast spinning-down of CTTSs to presently observed slow rotation during the first  $\sim 10^6$  years of their evolution. In the case of accreting, magnetized millisecond pulsars, the propeller mechanism may be responsible for relatively fast spinning-down during periods of lower accretion.

This work was supported in part by NASA grants NAG5-13220, NAG5-13060, NNG05GG77G, by NSF grants AST-0307817, AST-0507760 and by the CRDF grant KP2-2555-AL-03. AVK and G.V.U. were partially supported by the grant RFBR 06-02-16608.

## REFERENCES

- Aly, J.J. 1980, *A&A*, 86, 192  
 Aly, J.J., & Kuijpers, J. 1990, *A&A*, 227, 473–73  
 Balbus, S.A. 2003, *Enhanced Angular Momentum Transport in Accretion Disks*, *ARA&A*, 41, 555  
 Bisnovatyi-Kogan, G.S., & Komberg, B.V. 1974, *AZh*, 51, 373 (English trans. in *Soviet Astron.*, 18, 217 [1975])  
 Bisnovatyi-Kogan, G.S., & Ruzmaikin, A.A. 1976, *Astrophys. and Space Sci.*, 42, 401  
 Blandford, R.D., & Payne, D.G. 1982, *MNRAS*, 199, 883  
 Brio, M., & Wu, C.C. 1988, *Computat. Phys.*, 75, 400  
 Chandrasekhar, S. 1961, *Hydrodynamic and Hydromagnetic Stability* (Oxford: London), p. 273  
 Davidson, K., & Ostriker, J.P. 1973, *ApJ*, 179, 585  
 Davies, R.E., Fabian, A.C., & Pringle, J.E. 1979, *MNRAS*, 186, 779  
 Eksi, K. Y., Hernquist, L., & Narayan, R. 2005, *ApJ*, 623, L41–L44  
 Fendt, C., & Elstner, D. 2002, *A&A*, 363, 208  
 Ghosh P., & Lamb F.K. 1978, *ApJ*, 223, L83  
 Gold, T., & Hoyle, F. 1960, *MNRAS*, 120, 7  
 Goodson, A.P., Böhm, K.-H., & Winglee, R.M. 1999, *ApJ*, 199, 524, 142  
 Hayashi M., Shibata K., & Matsumoto R. 1996, *ApJ*, 468, L37  
 Illarionov, A.F., & Sunyaev, R.A. 1975, *A&A*, 39, 185  
 Ikhshanov, N.R. 2002, *A&A*, 381, L61  
 Kato, S., Fukue, J., & Mineshige, S. 1988, *Black-Hole Accretion Disks*, Kyoto University Press, Japan  
 Königl, A. 1991, *ApJ*, 370, L39  
 Lipunov, V.M. 1992, *Astrophysics of Neutron Stars*, Berlin: Springer Verlag  
 Lovelace, R.V.E., Berk H.L., & Contopoulos J., *ApJ*, 1991, 379, 696  
 Lovelace, R.V.E., Romanova M.M., & Bisnovatyi-Kogan G.S. 1995, *MNRAS*, 275, 244  
 Lovelace, R.V.E., Romanova M.M., & Bisnovatyi-Kogan G.S. 1999, *ApJ*, 514, 368 (LRBK99)  
 Lovelace, R.V.E., Li, H., Koldoba, A.V., Ustyugova, G.V., & Romanova, M.M. 2002, *ApJ*, 572, 455  
 Moffat, H.K. 1978, *Magnetic Field Generation in Electrically Conducting Fluids* (Cambridge: Cambridge University Press)  
 Rappaport, S. A., Fregeau, J. M., & Spruit, H. 2004, 606, 436  
 Rastätter, L. & Schindler, K. 1999, *ApJ*, 524, 361  
 Roe, P.L. 1986, *Ann. Rev. Fluid Mech.*, 18, 337  
 Romanova, M.M., Ustyugova, G.V., Koldoba, A.V., & Lovelace, R.V.E. 2002, *ApJ*, 578, 420  
 Romanova, M.M., Ustyugova, G.V., Koldoba, A.V., & Lovelace, R.V.E. 2003, *ApJ*, 595, 1009  
 Romanova, M.M., Ustyugova, G.V., Koldoba, A.V., & Lovelace, R.V.E. 2004a, *ApJ*, 610, 920  
 Romanova, M.M., Ustyugova, G.V., Koldoba, A.V., & Lovelace, R.V.E. 2004b, *ApJ*, 616, L151 (RUKL04)  
 Romanova, M.M., Ustyugova, G.V., Koldoba, A.V., & Lovelace, R.V.E. 2005, *ApJ*, 635, L165 (RUKL05)  
 Shakura, N.I., & Sunyaev R.A. 1973, *A&A*, 1973, 24, 337  
 Shu, F., Najita, J., Ostriker, E., Wilkin, F., Ruden, S., & Lizano, S. 1994, *ApJ*, 429, 781  
 Toth, G. 2000, *Computat. Phys.*, 161, 605  
 Ustyugova, G.V., Koldoba, A.V., Romanova, M.M., & Lovelace, R.V.E. 1999, *ApJ*, 516, 221  
 Ustyugova, G.V., Lovelace, R.V.E., Romanova, M.M., Li, H., & Colgate, S.A. 2000, *ApJ*, 541, L21  
 Uzdensky, D.A. 2002, *ApJ*, 572, 432  
 Uzdensky, D.A., Königl, A., & Litwin, C. 2002, *ApJ*, 565, 1205  
 Yelenina, T.G., & Ustyugova, G.V. 2005, preprint of the Keldysh Institute of Applied Mathematics, #16. (Submitted to *A&A*)